ABSTRACT

Surface Embedded Green Function Method Applied to Ag(111)

David A. Katz, M.S.

Advisor: Gregory A. Benesh, Ph.D.

Theoretical self-consistent calculations utilizing the Surface Embedded Green Function (SEGF) method have been performed on the Ag(111) surface. Analysis of the surface energetics reveal an energy minimum in the low temperature limit at an outerlayer contraction of 0.5% which agrees well with low energy electron diffraction and ion scattering studies. The predicted Ag(111) work function of 4.75 eV is in excellent agreement with the experimental value from photoelectron measurements. Furthermore, a surface state is predicted to exist at 0.15 eV below E_f, in very good agreement with a state observed experimentally in photoelectron spectroscopy at 0.12 eV below E_f. The best agreement with experiment across this diverse set of surface phenomena is obtained with the current implementation of the SEGF method.

Surface Embedded Green Function Method Applied to Ag(111)

by

David A. Katz, B.S.

A Thesis

Approved by the Department of Physics

_____

Gregory A. Benesh, Ph.D., Chairperson

Submitted to the Graduate Faculty of
Baylor University in Partial Fulfillment of the
Requirements for the Degree
of
Master of Science

Approved by the Thesis Committee

_____

Gregory A. Benesh, Ph.D., Chairperson

_____

Kenneth T. Park, Ph.D.

_____

Dwight P. Russell, Ph.D.

_____

Vincent S. Cronin, Ph.D.

Accepted by the Graduate School
August 2010

_____

J. Larry Lyon, Ph.D., Dean

Page bearing signatures is kept on file in the Graduate School.

TABLE OF CONTENTS

LIST OF FIGURES

LIST OF TABLES

ACKNOWLEDGMENTS

I thank Dr. Gregory Benesh for his guidance and support in helping me attain a level of understanding and competency in this field. I cherish our many conversations. I appreciated discussing with you not just the current state of theoretical condensed matter physics but how the field evolved from problems encountered in earlier approaches. I am appreciative of Dr. Kenneth Park, Nancy Yu, and Zhu Ke for including me in your discussions on experimental surface physics, design of experimental apparati, and analysis of experimental data. My sincere appreciation is extended to Dr. Dwight Russell and Dr. Vincent Cronin for their willingness to take time out of their schedules to serve on my thesis committee and for allowing me to share with them this work. Also, I want to thank the entire Physics faculty, fellow graduate students, and Baylor University for their support and kindness.

DEDICATION

To My Loving Wife

CHAPTER ONE

Introduction

Surface physics describes physical and chemical processes that occur in the first few atomic layers at the boundaries of solids. The surface region has proven to be unique, for the surface is the transition region from vacuum to solid and plays host to most interactions that solid bodies have with the external environment. On surfaces, one may observe the adsorption and diffusion of atoms, the photo-electric effect, and electron conduction. These phenomena are made possible by the unique electronic and chemical properties of the surface region.

The advent of Scanning Tunneling Microscopy (STM) in 1981 allowed us to probe matter at the atomic level became a reality, providing a boon to the field of surface physics. STMs have also made it possible to probe the local density of electron states in the surface region. Because processes involving surface adsorption can now be imaged experimentally, the field of surface physics has advanced rapidly. In the succeeding decades, surface physics has been concerned in large part with reconciling

images of the surface with our understanding of surface processes.

In addition to atomic-scale images of surfaces, the diversity in the types of surfaces encountered has increased rapidly as crystalline growth techniques have evolved. Molecular Beam Epitaxy (MBE) has enabled the study of heterogeneous inorganic structures. MBE permits the study of engineered surfaces which produce effects that are unobtainable with simple thermodynamic growth techniques.

Simultaneously, the semiconductor industry, a core constituent of the larger solid state community, has increased microchip speeds through scaling the manufacture of semiconductor components to smaller and smaller dimensions. As microchip dimensions involved for the construction of microchips have approached the 45 nm scale, it has been found that the performance of these chips can no longer be predicted without accounting for the influence of surface effects on microchip operation. The need for greater processor capabilities in industry has run headlong into surface physics; for a greater understanding of the unique electro-chemical environment of the surface region is required to adequately predict the behavior of these devices. Through the ability to manipulate and observe new

phenomena and the desire to predict the behavior of novel surfaces, further development of the theoretical basis of surface physics is required.

Theoretical surface physics is rooted in the density-functional theory (DFT) of Hohenberg, Kohn, and Sham[1,2]. Hohenberg and Kohn's theory[1] allows for the replacement of the many-body problem with an equivalent set of coupled single-body problems. Without such a simplification, the computational resources necessary to model even simple compounds would be extraordinary.

The many-body problem consists of a system of interacting electrons and ions, with a Hamiltonian given by:

$$H = T + T_I + V_{ext} + V_{\text{int}} + E_{II} \,. \tag{1.1}$$

The first term is the electron kinetic energy operator defined in atomic units as:

$$T = -\frac{1}{2}\sum_i \nabla_i^2 \,. \tag{1.2}$$

For ions with mass M_I the kinetic energy operator is defined as:

$$T_I = -\sum_I \frac{1}{2M_I}\nabla_I^2 \,. \tag{1.3}$$

The external potential generated by the ions that acts on electrons is defined by:

$$V_{ext} = -\sum_{i,I} \frac{Z_I}{\left|\vec{r}_i - \vec{R}_I\right|} . \qquad (1.4)$$

where $\vec{r}_i$ denotes the position of the i^{th} electron, Z_I denotes the charge of the I^{th} ion, and $\vec{R}_I$ is the position of the same ion.

The electron-electron interaction potential is defined as:

$$V_{\text{int}} = \frac{1}{2}\sum_{i \neq j} \frac{1}{\left|\vec{r}_i - \vec{r}_j\right|} . \qquad (1.5)$$

Lastly, the ion-ion interaction potential is defined as:

$$E_{II} = \frac{1}{2}\sum_{I \neq J} \frac{Z_I Z_J}{\left|\vec{R}_I - \vec{R}_J\right|} . \qquad (1.6)$$

The Hohenberg-Kohn theory[1] states that for any system of interacting particles in a static external potential (thus, $T_I = 0$), there exists a universal functional for the energy in terms of the particle density $n(\vec{r})$. The ground state energy of the interacting system E_0, is the global minimum of this energy functional, and the density that minimizes this functional is the ground state particle density $n_0(\vec{r})$.

In solid state physics applications, we seek to replace the many-body Hamiltonian of a system of interacting electrons with a single body equation for the charge density with an effective Hamiltonian. However, no exact representation of the energy functional has been found for electrons in an arbitrary configuration. The inability to find the energy functional is due to the exchange and correlation effects exhibited by pairs of electrons.

Representations for the energy functional are known for certain electronic configurations, most notably the homogeneous electron gas. Kohn and Sham[2] utilized this success and created an approximation for the exchange correlation effects via the Local Density Approximation (LDA). To do so requires assuming that the ground state density can be represented by the ground state of an auxiliary system of non-interacting particles, and that the auxiliary Hamiltonian possesses an effective local potential.

In the LDA, the form of the effective local potential is the sum of the ordinary columbic potential and a new exchange-correlation potential found from the homogeneous gas of the same particle density as the average particle

density of the local region of interest. The electrostatic coulomb potential is defined as:

$$V_{es}(\rho,\vec{r}) = \int d^3r' \frac{\rho(\vec{r}')}{|\vec{r}-\vec{r}'|} - \sum_I \frac{Z_I}{|\vec{r}-\vec{R}_I|} . \quad (1.7)$$

The LDA exchange correlation potential is:

$$V_{xc}(\vec{r}) = \varepsilon_{xc}([\rho],\vec{r}) + \rho(\vec{r}) \frac{\delta\varepsilon_{xc}([\rho],\vec{r})}{\delta\rho(\vec{r})} , \quad (1.8)$$

where ε_{xc} is the exchange energy per electron, and for an unpolarized electron gas is:

$$\varepsilon_x([\rho],\vec{r}) = -\frac{3}{4}\left(\frac{3\rho(\vec{r})}{\pi}\right)^{\frac{1}{3}} . \quad (1.9)$$

Thus, the effective Hamiltonian may be written as:

$$H_{eff} = T + V_{es} + V_{xc} + E_{II} . \quad (1.10)$$

By taking the expectation value of H_{eff} we find the energy functional; and by minimizing this expectation value with respect to density variations, we may find the ground state charge density, $\rho_0(\vec{r})$, defined as:

$$\rho_0(\vec{r}) = \sum_i |\psi_i(\vec{r})|^2 , \quad (1.11)$$

where

$$\left[T + V_{es} + V_{xc}\right]\psi_i = E_i\psi_i , \quad (1.12)$$

and the sum is over all occupied states. Equation (1.12) represents the one-electron-like Schrödinger equation.

DFT-LDA forms the basis for theoretical surface calculations, and though no formal proof has been offered to support the LDA, its ability to accurately model electronic systems has been verified in a great many computational studies.

Though DFT theory is an exact theory, the LDA is not. When the charge density varies greatly, or if strongly correlated pairs of electrons exist, the LDA exhibits computational errors. For charge density variations, gradient corrections may be added to improve the approximation, but there is a cost in the loss of the local character in the potential. Near atomic centers, charge density variations become too great for even gradient corrections. However, near these atomic centers we may approximate the potential as only varying radially, thus recovering the ability to solve the Dirac equation directly. Strongly correlated systems of electrons, like those found in solids containing partially-filled d- and f-bands, violate the LDA because electrons in d- and f- band orbitals are spatially confined and strong columbic repulsion exists, giving rise to an underestimated correlation effect. Modifications of the LDA to include these effects produce the so-called LDA+U methods.

Application of the DFT-LDA methodology to surfaces introduces no new sources of error other than those found for solids. Since the charge density in the vacuum region is slowly-varying, the vacuum region charge density is well represented by the LDA. The greatest challenge to modeling surfaces is not DFT or the LDA, but adequately representing the electronic environment without excessive computational demand.

CHAPTER TWO

Method

A. Theoretical Techniques of Surface Physics

Slab and slab super-cell geometries are commonly used in surface calculations. These geometries place atomic cores in two-dimensional slabs running parallel to the desired surface and stacked in the normal direction. One limitation of theoretical studies based on slab geometries is the inadequate number of layers used to represent the bulk. Solids are typically millions of layers deep, not the 5-20 layers commonly used in slab calculations. Thin slabs only crudely approximate the environment of the surface, and the limitations are clearly observed in the inaccuracy of the density of states produced from such methods.

In solids, the splitting of electronic degeneracies from the exclusion principle causes electrons to exist in continua of states, called electronic bands. The small number of layers utilized in slab methods proves insufficient for describing states with a wavevector component normal to the surface, and rather than forming band continua, only discrete levels exist instead.

To avoid the pitfalls associated with traditional slab-based methods, the alternative technique of the Surface Embedded Green Function (SEGF) was developed.[3,4] The objective was to more closely model the surface environment, without increasing computational expense, by embedding a slab onto the semi-infinite bulk crystal. The approximation employed in the SEGF method is that, at a certain depth from the vacuum-surface interface, the crystal becomes bulk-like. In situations where there exists adequate free electron density (as found in metals), effective screening of the surface occurs over a short range, and bulk-like character is regained in a few atomic layers. The advantages of such an approach is that accurate charge densities, densities of states, and work functions may be calculated with significantly less computational demand, since 3-layer SEGF calculations typically compete in accuracy with 15-20 layer slabs.[5]

B. The SEGF Method

The SEGF method divides the crystal into two regions: the surface (which includes several atomic layers and the vacuum region just outside the crystal) and the bulk substrate. The method assumes that the bulk wave function $\psi(\vec{r})$ is given and is exact, since it may be derived from

solving the Schrödinger equation using other methods (e. g. MJW, WIEN2k). We seek to find the surface region wave function, $\phi(\vec{r})$, that matches onto $\psi(\vec{r})$ over the embedding surface S. This is accomplished by minimizing the energy expectation value with respect to variations in $\phi(\vec{r})$. Figure 2. 1 depicts the way in which space is divided to solve the Schrödinger equation for $\phi(\vec{r})$.

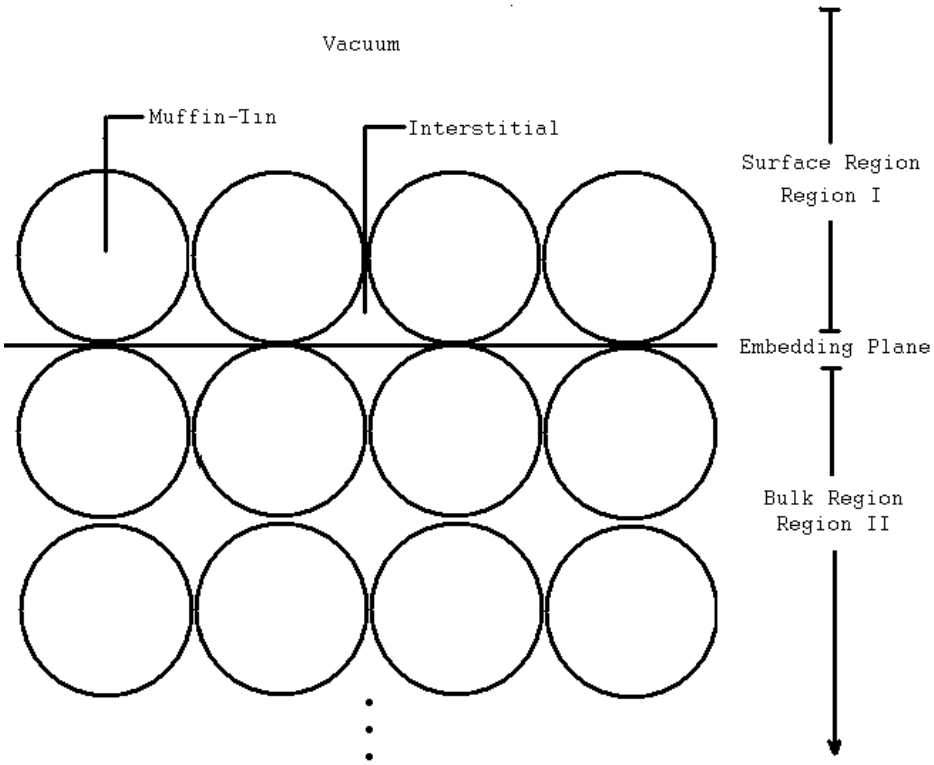

Figure 2.1: The semi-infinite crystal. Region I includes the vacuum, surface muffin-tin spheres, and interstice, and region II contains the truncated bulk substrate.

To minimize the energy with respect to $\phi(\vec{r})$, we must first express the energy in terms of $\phi(\vec{r})$ and the bulk Green function. From the time-independent Schrödinger equation we have:

$$E = \frac{<\Phi(\vec{r})|H|\Phi(\vec{r})>}{<\Phi(\vec{r})|\Phi(\vec{r})>}, \qquad (2.1)$$

$$\text{where } \Phi(\vec{r}) \equiv \begin{Bmatrix} \phi(\vec{r}) \text{ in the surface region} \\ \psi(\vec{r}) \text{ in the bulk region} \end{Bmatrix}.$$

Expanding equation (2.1) in atomic units, we obtain:

$$E = \frac{\int_I d^3r\, \phi^* H\phi + \varepsilon \int_{II} d^3r\, |\psi|^2 + \frac{1}{2}\iint_s d^2r_s\, \phi^* \frac{\partial \phi}{\partial n_s} - \frac{1}{2}\iint_s d^2r_s\, \varphi^* \frac{\partial \psi}{\partial n_s}}{\int_I d^3r\, |\varphi|^2 + \int_{II} d^3r\, |\psi|^2}. \qquad (2.2)$$

To obtain an expression for E in terms of the region I trial function $\phi(\vec{r})$, we must rewrite terms involving $\psi(\vec{r})$. These are the terms containing the normal derivative of the wave function $\psi(\vec{r})$ at the surface and the probability amplitude integrals for $\psi(\vec{r})$.

For terms involving the surface integral of $\frac{\partial \psi}{\partial n_s}$, we utilize the properties of the bulk Green function at the interface. To illustrate, $\psi(\vec{r})$ satisfies Schrödinger's equation in the bulk region:

$$\left[-\frac{1}{2}\nabla^2 + V(\vec{r}) - \varepsilon\right]\psi(r) = 0. \qquad (2.3)$$

Thus, the bulk Green function satisfies:

$$\left[-\frac{1}{2}\nabla^2 + V(\vec{r}) - \varepsilon\right] G_o(\vec{r},\vec{r}') = \delta(\vec{r}-\vec{r}') \,. \qquad (2.4)$$

Multiplying equation (2.3) by $G_o(\vec{r},\vec{r}')$ and (2.4) by $\psi(\vec{r})$, Subtracting, and integrating over the bulk volume we obtain:

$$\psi(\vec{r}) = \frac{1}{2}\int_{II} d^3\vec{r}' \left[G_o(\vec{r},\vec{r}')\nabla^2\psi(\vec{r}') - \psi(r)\nabla^2 G_o(\vec{r},\vec{r}')\right]. \qquad (2.5)$$

The application of Green's Theorem yields:

$$\psi(\vec{r}) = -\frac{1}{2}\iint_s d^2\vec{r}_s \left[G_0(\vec{r}_s,\vec{r}\,')\frac{\partial\psi(\vec{r}_s)}{\partial n_s} - \psi(\vec{r}_s)\frac{\partial G_0(\vec{r}_s,\vec{r}\,')}{\partial n_s}\right]. \qquad (2.6)$$

Neumann boundary conditions are imposed on the interface plane of the bulk substrate, namely:

$$\frac{\partial G_0(\vec{r},\vec{r}_s')}{\partial n_s} = 0 \,.$$

On the embedding plane, equation (2.6) reduces to:

$$\psi(\vec{r}_s) = -\frac{1}{2}\iint_s d^2\vec{r}_s' G_0(\vec{r}_s,\vec{r}_s')\frac{\partial\psi(\vec{r}_s')}{\partial n_s} \,. \qquad (2.7)$$

Inverting equation (2.7) gives:

$$\frac{\partial\psi}{\partial n_s} = -2\iint_s d^2\vec{r}_s' G_0^{-1}(\vec{r}_s,\vec{r}_s')\psi(\vec{r}_s') \,.$$

Since Φ is assumed to be continuous on the boundary, $\psi(\vec{r}_s') = \phi(\vec{r}_s')$. Thus, $\frac{\partial\psi}{\partial n_s}$ may be expressed as:

$$\frac{\partial \psi(r_s)}{\partial n_s} = -2\iint_s d^2\vec{r}_s' G_0^{-1}(\vec{r}_s, \vec{r}_s')\varphi(\vec{r}_s') \,. \qquad (2.8)$$

To rewrite the probability amplitude integrals over region II, the complex conjugate of the Schrödinger equation in the bulk region is multiplied by a variation in $\psi(\vec{r})$, yielding:

$$\delta\psi H\psi^* = \varepsilon\psi^*\delta\psi \,. \qquad (2.9)$$

Variation of the bulk Schrödinger equation with respect to energy and $\psi(\vec{r})$ results in:

$$H\delta\psi = \psi\delta\varepsilon + \varepsilon\delta\psi \,. \qquad (2.10)$$

Multiplication by $\psi^*(\vec{r})$ yields:

$$\psi^* H\delta\psi = \psi^*\psi\delta\varepsilon + \varepsilon\psi^*\delta\psi \,. \qquad (2.11)$$

Subtracting equation (2.9) from equation (2.11) gives:

$$\psi^* H\,\delta\psi - \delta\psi\, H\,\psi^* = \psi^*\psi\,\delta\varepsilon \,. \qquad (2.12)$$

Isolating the modulus squared and integrating over the volume gives the probability amplitude integral:

$$\begin{aligned}\int_{II} d^3\vec{r}\,\psi^*(\vec{r})\psi(\vec{r}) &= \int_{II} d^3\vec{r}\left[\psi^*(\vec{r})H\frac{\delta\psi(\vec{r})}{\delta\varepsilon} - \frac{\delta\psi(\vec{r})}{\delta\varepsilon}H\psi^*(\vec{r})\right] \\ &= -\frac{1}{2}\int_{II} d^3\vec{r}\left[\psi^*(\vec{r})\nabla^2\frac{\delta\psi(\vec{r})}{\delta\varepsilon} - \frac{\delta\psi(\vec{r})}{\delta\varepsilon}\nabla^2\psi^*(\vec{r})\right]\end{aligned} \,. \qquad (2.13)$$

Next, utilizing Green's Identity and noting again that at the surface $\psi(\vec{r}_s') = \phi(\vec{r}_s')$ we obtain:

$$\int_{II} d^3r\,\psi^*\psi = \frac{1}{2}\iint_s d^2\vec{r}_s\left[\phi^*(\vec{r}_s)\frac{\partial}{\partial\varepsilon}\frac{\partial\psi(\vec{r}_s)}{\partial n_s} - \frac{\partial\phi(\vec{r}_s)}{\partial\varepsilon}\frac{\partial\psi^*(\vec{r}_s)}{\partial n_s}\right]. \qquad (2.14)$$

Substituting from equation (2.8), for $\frac{\partial \psi}{\partial n_s}$ we conclude:

$$\int_{II} d^3\vec{r}\,\psi^*\psi = -\iint_s d^2\vec{r}_s' \iint_s d^2\vec{r}_s \left[\phi^*(\vec{r}_s) \frac{\partial G_0^{-1}(r_s, r_s')}{\partial \varepsilon} \phi(\vec{r}_s') \right]. \qquad (2.15)$$

The expressions from equations (2.15) and (2.8) are substituted into (2.2) to obtain the energy in terms of the bulk Green function and the trial wave function in the surface region:

$$E = \frac{\int_I d^3\vec{r}\,\phi^* H \phi + \frac{1}{2}\iint_s d^2\vec{r}_s \phi^*(r_s) \frac{\partial \phi}{\partial n_s} + \iint_s d^2\vec{r}_s \iint_s d^2\vec{r}_s' \phi^*(\vec{r}_s') \left(G_0^{-1} - \varepsilon \frac{\partial G_0^{-1}}{\partial \varepsilon} \right) \phi(\vec{r}_s')}{\int_I d^3\vec{r}\,|\varphi|^2 - \iint_s d^2\vec{r}_s \iint_s d^2 r_s'' \phi^*(\vec{r}_s) \frac{\partial G_0^{-1}}{\partial \varepsilon} \phi(\vec{r}_s')}. \qquad (2.16)$$

We choose to represent $\phi(\vec{r})$ in terms of the Linearized Augmented Plane Wave[6] (LAPW) basis set, $\{\chi_i(\vec{r})\}$, and minimize E with respect to the set of coefficients, $\{a_i\}$, in the LAPW expansion of $\phi(\vec{r})$. Expanding equation (2.16) in this basis and evaluating for the special k-point denoted by $\vec{K}$, yields the following matrix representation for the effective Schrödinger equation in the surface region:

$$\sum_j \left[H_{ij} + \left(G_{0,\vec{K}}^{-1} \right)_{ij} + (E - \varepsilon) \frac{\partial (G_{0,\vec{K}}^{-1})_{ij}}{\partial \varepsilon} \right] a_j = E \sum_j O_{ij} a_j \,, \qquad (2.17)$$

where

$$H_{ij} = \iiint d^3 r\, \chi_i^*(\vec{r}) H \chi_j(\vec{r}) + \frac{1}{2} \iint d^2 r_s\, \chi_i^*(\vec{r}_s) \frac{\partial \chi_j(\vec{r})}{\partial n_s}, \qquad (2.18)$$

$$(G_{0,\vec{K}}{}^{-1})_{ij} = \iint d^2 r_s \iint d^2 r_s'\, \chi_i^*(\vec{r}_s) G_{0,\vec{K}}{}^{-1}(\vec{r}_s, \vec{r}_s') \chi_j^*(\vec{r}'_s), \qquad (2.19)$$

and

$$O_{ij} = \iiint d^3 r\, \chi_i^*(\vec{r}) \chi_j(\vec{r}). \qquad (2.20)$$

Now, the surface Green function, $G_{\vec{K}}(r, r', E)$, may be calculated by solving the analogous equation:

$$\sum_k \left[H_{ik} + \left(G_{0,\vec{K}}{}^{-1}\right)_{ik} + (E - \varepsilon) \frac{\partial (G_{0,\vec{K}}{}^{-1})_{ik}}{\partial \varepsilon} - E O_{ik} \right] g_{kj}(\varepsilon) = \delta_{ij}, \qquad (2.21)$$

where,

$$G_{\vec{K}}(r, r', E) = \sum_{i,j} g_{ij}(E) \chi_i^*(\vec{r}) \chi_j(\vec{r}). \qquad (2.22)$$

By evaluating at $\varepsilon = E$, equation (2.21) is reduced to:

$$\sum_k [H_{ik} + (G_{0,\vec{K}}{}^{-1})_{ik} - E O_{ik}]\, g_{kj}(E) = \delta_{ij}. \qquad (2.23)$$

O_{ik} is completely defined from the choice of the basis, and $G_{0,\vec{K}}{}^{-1}$ is obtained from the scattering properties of the bulk crystal for planar geometries or through self-consistent calculations[7,8]. It may be evaluated independently of the surface calculation. $G_{0,\vec{K}}{}^{-1}$ contains the influence of the bulk region on the surface and can be thought of as an embedding potential. However, H_{ik} matrix

elements contain the effective local potential, which depends on the surface charge density. If the potential were known to great accuracy, the solution of equation (2.22) would follow directly. Once the matrix equation is solved for $g_{kj}(E)$, the charge density may be obtained by integrating the imaginary part of $G_{\vec{K}}(r,r',E)$ up to the Fermi energy:

$$\rho(\vec{r}) = \sum_{\vec{K}} \rho_{\vec{K}}(\vec{r}) = \sum_{i,j,\vec{K}} \chi_i^{*}(\vec{r})\chi_j(\vec{r}) \frac{1}{\pi} \int_{-\infty}^{E_f} dE \, \mathrm{Im}\left\{ \frac{1}{2i} \left[g_{ij}(E+i\varepsilon) - g_{ij}^{*}(E-i\varepsilon) \right] \right\} . \tag{2.24}$$

Similarly, the density of states may also be obtained as:

$$\sigma(E) = \sum_{\vec{K}} \sigma_{\vec{K}}(E) = \sum_{i,j,\vec{K}} \frac{1}{\pi} \int d^3r \; \chi_i^{*}(\vec{r}) \, \chi_j(\vec{r}) \, \mathrm{Im}\left\{ \frac{1}{2i} \left[g_{ij}(E+i\varepsilon) - g_{ij}^{*}(E-i\varepsilon) \right] \right\} . \tag{2.25}$$

Since the potential is not known to arbitrary accuracy, we solve (2.23) self-consistently. An initial guess for the charge density produces an electrostatic potential as the solution of Poisson's equation. The exchange-correlation terms are computed and then added to the electrostatic potential. The Hamiltonian is then formed and the surface Green function obtained by solving equation (2.23). The output charge density is then computed via equation (2.24). This process is repeated until consistency between input and output charge density

is achieved. To keep the iteration process stable, the output charge density is mixed with the input charge density to form a new input charge density. The process is diagrammatically outlined in Figure 2.2.

C. Choice of Basis

As illustrated in Figure 2.1, the surface region geometry is composed of three unique sub-regions: the vacuum, muffin-tin, and interstitial regions. We seek to find a basis set of functions that can accurately represent surface wavefunctions in all three regions. An important consideration is the quadratic increase in the number of matrix elements to be calculated and the cubic increase in computational time caused by increasing basis size. Thus, a set of basis functions is sought which is capable of high accuracy with minimal size. The Linearized Augmented Plane Wave (LAPW) basis was chosen to expand the charge density, because this basis can accurately represent the charge density in each sub-region with reasonable size.[6]
The LAPW basis functions are piecewise defined in each sub-region and are continuous with continuous derivatives everywhere, including across the bounding surface of the sub-regions. The piecewise definition of the basis allows

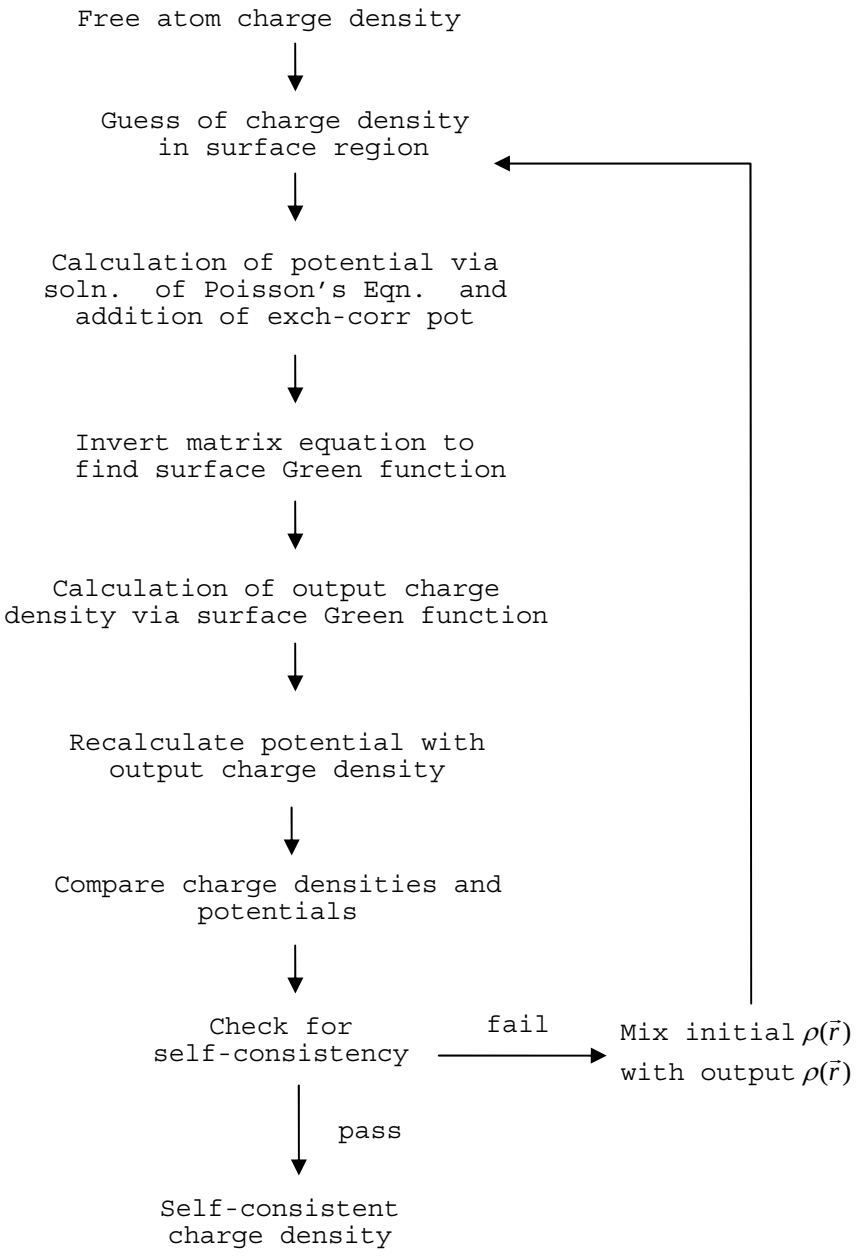

Figure 2.2: Programmatic diagram of the self-consistent calculation.

freedom to choose an appropriate basis for each unique sub-region.

Since the interstitial region has a slowly-varying charge density, an expansion in plane waves will converge quickly to the actual charge density. Plane waves with high wave numbers may largely be neglected, as these waves contribute to variations over shorter distances. Further, a plane wave expansion simplifies the solution of Poisson's equation and the evaluation of matrix elements.

The interstitial plane wave basis functions are:

$$\chi_{mn}(\vec{r}) = \begin{cases} \sqrt{\frac{2}{\Omega}} e^{i\vec{K}_m \bullet \vec{r}} \cos(k_n z) & \text{even symmetry} \\ \sqrt{\frac{2}{\Omega}} e^{i\vec{K}_m \bullet \vec{r}} \sin(k_n z) & \text{odd symmetry} \end{cases} \qquad (2.26)$$

where $\vec{K}_m$ is a wave vector defined by $\vec{K}_m = \vec{K} + \vec{G}_m$ and $\vec{G}_m$ is a reciprocal lattice vector, $\vec{k}_n = \frac{n\pi}{\tilde{d}}\hat{z}$ where $\tilde{d}$ is slightly larger than the slab thickness, and Ω is the volume of the surface region.

Inside the muffin-tins, plane wave expansions will not converge quickly, for near the atomic cores the charge density changes rapidly. However, a model potential and Hamiltonian can be constructed to generate the basis functions for the expansion of the actual charge density and potential in the muffin-tin.

The model potential is constructed by taking the spherically-averaging the muffin-tin potential from the prior SEGF cycle. The shape approximation made in generating the model potential facilitates solution, for in spherical coordinates with a potential possessing only radial dependence, the Schrödinger equation may be written as:

$$\left[-\frac{1}{2}\frac{\partial^2}{\partial r^2}+\frac{\hat{L}^2}{2r^2}+V(r)\right]\chi'(\vec{r})=E\ \chi'(\vec{r}) \qquad (2.27)$$

where,

$$\hat{L}^2=\frac{1}{\sin^2\theta}\left[\sin\theta\frac{\partial}{\partial\theta}\left(\sin\theta\frac{\partial}{\partial\theta}\right)+\frac{\partial^2}{\partial\varphi^2}\right]. \qquad (2.28)$$

Then utilizing separation of variables, we obtain from the angular equations the spherical harmonic solutions $Y_{lm}(\theta,\varphi)$, and from the radial equation we may obtain the radial solution $u_L(r)$ from:

$$\left[-\frac{1}{2}\frac{\partial^2}{\partial r^2}+\frac{l(l+1)}{2r^2}+V(r)\right]u_L(r)=E_L\ \ u_L(r), \qquad (2.29)$$

where L is the collective angular momentum index.
The basis functions are then:

$$\chi(\vec{r})=u_L(r,E)Y_L(\theta,\varphi)i^l\ . \qquad (2.30)$$

In general, this function will not match onto the interstitial basis in both value and slope at the muffin-tin boundary. Thus, additional freedom must be included in

the basis. If a linear combination of such functions with differing L, augmented with a linear combination of energy-derivative radial solutions is used, then sufficient variational freedom is obtained. The linear combination may be chosen such that the boundary conditions are satisfied at the muffin-tin radius. So, for each inequivalent atom, the basis functions inside the muffin-tin are given by:

$$\chi_{mn}(\vec{r}) = \begin{cases} \sum_L \left[A_L(\vec{K}^{+}_{mn}) u_L(r, E_L) + B_L(\vec{K}^{+}_{mn}) \dot{u}_L(r, E_L) \right] Y_L(\vartheta, \phi) i^l & \text{even sym.} \\ \sum_L \left[A_L(\vec{K}^{-}_{mn}) u_L(r, E_L) + B_L(\vec{K}^{-}_{mn}) \dot{u}_L(r, E_L) \right] Y_L(\vartheta, \phi) i^{l-1} & \text{odd sym.} \end{cases}, \quad (2.31)$$

where $\vec{K}^{\pm}_{mn} = \vec{K}_m \pm k_n \hat{z}$. The energy derivative $\dot{u}_L$ functions are included to provide variational freedom over a range of energies, not merely at energy E_L.

The vacuum region exhibits periodic symmetry in the two dimensions running parallel to the surface. Perpendicular to the surface the model potential depends only on the normal coordinate z. The model potential is constructed on a linear mesh in z. From the planar-averaged potential of the prior SEGF cycle, the basis functions are found by solving Schrödinger's equation in vacuum with the model potential. Plane waves accurately represent the slowly varying x- and y-dependence of surface wave functions, since they are solutions of the Schrödinger

equation with a constant potential. The z-dependent portion of the basis functions are solutions of:

$$\left[-\frac{1}{2}\frac{d^2}{dz^2}-\frac{K_m{}^2}{2}+V(z)\right]v_m(z,E_z)=E_z\ v_m(z,E_z)\,, \qquad (2.32)$$

where, $K_m{}^2=\left|\vec{K}+\vec{G}_m\right|^2$ and E_z is chosen to be near the Fermi energy.

The vacuum region's basis functions must also have sufficient variational freedom in energy. This is accomplished by adding energy derivative solutions $\dot{v}_m$ to our basis. This produces a basis set that is reasonably complete over an energy range about $E=E_z$. Thus,

$$\chi_{mn}(\vec{r})=\left[\alpha_{mn}v_m(z,E_z)+\beta_{mn}\dot{v}_m(z,E_z)\right]e^{i\vec{K}_m\bullet\vec{r}}\,. \qquad (2.33)$$

D. The Charge Density

The expansion coefficients for the surface Green function are calculated by inverting equation (2.23). By applying the basis definition in equation (2.24), the expansion coefficients for the charge density in each sub-region may be expressed in terms of the integral of the surface Green function coefficients.

For the interstitial region, the charge density is expanded in plane waves as:

$$\rho(\vec{r}) = \sum_{\vec{K}} \rho_{\vec{K}}(\vec{r}) = \sum_{mn} \rho_{mn} \sqrt{\frac{2}{\Omega}} e^{i\vec{G}_m \bullet \vec{r}} \begin{Bmatrix} \cos(k_n z) \\ \sin(k_n z) \end{Bmatrix} . \qquad (2.34)$$

From equation (2.24) and the basis, $\rho_{\vec{K}}(\vec{r})$ is found to be:

$$\rho_{\vec{K}}(\vec{r}) = \sum_{i,j} \frac{1}{\pi} e^{i(\vec{K}_{m'} - \vec{K}_m) \bullet \vec{r}} \begin{Bmatrix} \cos(k_{n'} z) \\ \sin(k_{n'} z) \end{Bmatrix} \begin{Bmatrix} \cos(k_n z) \\ \sin(k_n z) \end{Bmatrix} \hat{G}_{m'n',mn} \qquad (2.35)$$

where,

$$\hat{G}_{m'n',mn} \equiv \int_{-\infty}^{E_f} dE \, \mathrm{Im} \left\{ \frac{1}{2i} \left[g_{ij}(E + i\varepsilon) - g_{ij}{}^{*}(E - i\varepsilon) \right] \right\} . \qquad (2.36)$$

The expansion coefficient ρ_{mn} can now be expressed by equating equations (2.34) and (2.35); this gives:

$$\rho_{m''n''} = \frac{1}{\Omega} \sum_{mn \geq m'n'} \sum_{m'n;} f \left[\hat{G}_{m'n',mn} \, \delta_{m'',m'-m} + \hat{G}^{*}{}_{m'n',mn} \, \delta_{m'',m-m'} \right] \begin{Bmatrix} \delta_{n'',|n'-n|} \pm \delta_{n'',|n'+n|} \\ \delta_{n'',n'+n} \pm \delta_{n'',|n'-n|} \end{Bmatrix} \qquad (2.37)$$

where, $f = \frac{1}{2}$ if $m'n' = mn$ or $f = 1$, otherwise.

Inside the muffin-tins, the charge density is expanded as:

$$\rho_{\vec{K}}(\vec{r}) = \sum_{L,\vec{K}} \rho_{L,\vec{K}}(r) Y_L(\theta, \phi) . \qquad (2.38)$$

The expansion coefficient $\rho_{L,\vec{K}}(r)$ can be found in terms of the surface Green function by expanding equation (2.24) and equating this to equation (2.38). This process yields:

$$\rho_{L'',\vec{K}}(r) = \left[C^1_{L',L} u_{L'}(r) u_L(r) + C^2_{L',L} \dot{u}_{L'}(r) \dot{u}_L(r) + C^3_{L',L} \dot{u}_{L'}(r) u_L(r) + C^4_{L',L} \dot{u}_{L'}(r) u_L(r) \right] \iint d\Omega Y_{L'} Y_L^{*} Y_{L''}^{*} \qquad (2.39)$$

where,

$$C^1_{L',L} = \sum_{mn\geq m'n'} \sum_{m'n'} f\,[\hat{G}_{m'n',mn}\tilde{A}_{L'}{}^{\pm}(\vec{K}_{m'n'})\tilde{A}^{*\pm}_{L}(\vec{K}_{mn}) + \hat{G}^{*}_{m'n',mn}\tilde{A}_{L'}{}^{\pm}(\vec{K}_{mn})\tilde{A}^{*\pm}_{L}(\vec{K}_{m'n'})]$$

$$C^2_{L',L} = \sum_{mn\geq m'n'} \sum_{m'n'} f\,[\hat{G}_{m'n',mn}\tilde{B}_{L'}{}^{\pm}(\vec{K}_{m'n'})\tilde{B}^{*\pm}_{L}(\vec{K}_{mn}) + \hat{G}^{*}_{m'n',mn}\tilde{B}_{L'}{}^{\pm}(\vec{K}_{mn})\tilde{B}^{*\pm}_{L}(\vec{K}_{m'n'})]$$

$$C^3_{L',L} = \sum_{mn\geq m'n'} \sum_{m'n'} f\,[\hat{G}_{m'n',mn}\tilde{A}_{L'}{}^{\pm}(\vec{K}_{m'n'})\tilde{B}^{*\pm}_{L}(\vec{K}_{mn}) + \hat{G}^{*}_{m'n',mn}\tilde{A}_{L'}{}^{\pm}(\vec{K}_{mn})\tilde{B}^{*\pm}_{L}(\vec{K}_{m'n'})]$$

$$C^4_{L',L} = \sum_{mn\geq m'n'} \sum_{m'n'} f\,[\hat{G}_{m'n',mn}\tilde{B}_{L'}{}^{\pm}(\vec{K}_{m'n'})\tilde{A}^{*\pm}_{L}(\vec{K}_{mn}) + \hat{G}^{*}_{m'n',mn}\tilde{A}_{L'}{}^{\pm}(\vec{K}_{mn})\tilde{B}^{*\pm}_{L}(\vec{K}_{m'n'})]\,.$$

Here, $\tilde{A}_L{}^{\pm}(\vec{K}_{mn})$ is defined as:

$$\tilde{A}_L{}^{\pm}(\vec{K}_{mn}) = \begin{cases} i^l A_L(K^+_{mn}) & \text{for even n} \\ i^{l-1} A_L(K^-_{mn}) & \text{for odd n} \end{cases},$$

and a similar expression defines $\tilde{B}_L{}^{\pm}(\vec{K}_{mn})$.

The vacuum charge density is expanded as:

$$\rho_{\vec{K}}(r) = \sum_{mn} \rho_m(z) e^{i\vec{G}_m \bullet \vec{R}}\,, \qquad (2.40)$$

where $\rho_m(z) = \gamma_m\left[\alpha_{mn}\nu_m(z,E_z) + \beta_{mn}\dot{\nu}_m(z,E_z)\right]$.

The $\rho_m(z)$ coefficients are obtained by equating equation (40) to the energy integration of the Green function in the vacuum basis, and are found to be:

$$\rho_{m''}(z) = \sum_{mn\geq m'n'} \sum_{mn} f\left[\hat{G}_{m'n',mn}\delta_{m'',m'-m} + \hat{G}^{*}_{m'n',mn}\delta_{m'',m-m'}\right]\left[\alpha_{mn}\nu_m(z,E_z) + \beta_{mn}\dot{\nu}_m(z,E_z)\right] \times\left[\alpha_{m'n'}\nu_{m'}(z,E_z) + \beta_{m'n'}\dot{\nu}_{m'}(z,E_z)\right]. \qquad (2.41)$$

E. The Electrostatic Potential

The electrostatic potential is obtained by solving Poisson's equation in each of the three sub-regions. The

process is greatly facilitated by expanding the potential in the same basis as the charge density. In the vacuum region, the charge density is given by equation (2.40). The electrostatic potential is expanded similarly as:

$$V_{vac}(\vec{r}) = \sum_m V_m(z) e^{i\vec{G}_m \bullet \vec{r}} \ . \qquad (2.42)$$

Equation (2.42) is substituted into Poisson's equation, and the following differential equation for $V_m(z)$ in terms of $\rho_{\bar{K}}(z)$ is obtained:

$$-\frac{d^2}{dz^2} V_m(z) + G_m{}^2 V_m(z) = 4\pi \rho_{\bar{K}}(z) \ . \qquad (2.43)$$

Equation (43) is solved numerically for $V_m(z)$ under the boundary conditions that the electrostatic potential goes to a constant as z tends to $-\infty$, and that it matches in value and slope to the interstitial potential at the vacuum-interstitial plane. By considering the m=0 case, we find a free constant which is the value the electrostatic potential takes at large distances, denoted as the vacuum constant ϕ_0. The difference between the Fermi energy, the highest occupied energy state, and ϕ_0 gives the minimum energy required to remove an electron from the surface, which is defined as the work function. For other values of m, another constant emerges, denoted as C_m, which will aid

in matching the potential solution in the vacuum region to the interstitial potential.

In the interstitial region, the electrostatic potential arises from the charge residing in all three sub-regions. The contribution from the charge inside the muffin-tin spheres may be computed through a multipole expansion. The electrostatic potential outside a sphere due to a localized charge distribution ρ_{MT} inside the sphere is given by:

$$V(\vec{r}) = \sum_{l=0}^{\infty} \frac{4\pi}{2l+1} q_{lm} \frac{Y_{lm}(\theta,\phi)}{r^{l+1}}, \qquad (2.44)$$

where q_{lm} is the multipole moment of the charge density. Since the potential is determined from the multipole expansion of the charge density, and not the actual charge density itself, a pseudo-charge density $\tilde{\rho}_{MT}(\vec{r})$ may be substituted for the actual charge density in the muffin-tin spheres, so long as it possesses the same multipole moments. Using the pseudo-charge method of Weinert[9], the charge density in the muffin-tins is expanded in plane waves. The pseudo-charge expansion coefficients $\{\tilde{\rho}_{mn}\}$ are chosen so as to reproduce the actual multipoles of the charge distribution. Thus, the contribution to the potential generated by $\tilde{\rho}_{MT}(\vec{r})$ in the interstitial region is

identical to that generated by the actual charge density. The charge density used to calculate the electrostatic potential in the interstitial region is:

$$\tilde{\rho}(\vec{r}) = \rho_{\text{int}}(\vec{r}) + \tilde{\rho}_{MT}(\vec{r}) \tag{2.45}$$

where, $\tilde{\rho}_{MT}(\vec{r}) = \sum_{\vec{K}} \tilde{\rho}_{mn} e^{i\vec{G}_m \bullet \vec{r}} \begin{cases} \cos(k_n z) & \text{even sym.} \\ \sin(k_n z) & \text{odd sym.} \end{cases}$,

and $\rho_{\text{int}}(\vec{r}) = \sum_{\vec{K}} \rho_{mn} e^{i\vec{G}_m \bullet \vec{r}} \begin{cases} \cos(k_n z) & \text{even sym.} \\ \sin(k_n z) & \text{odd sym.} \end{cases}$.

Now, $\tilde{\rho}(\vec{r})$ is inserted into Poisson's equation and the equation is solved over the whole unit cell (interstitial and muffin-tin) for the electrostatic potential, $V_{\text{int}}(\vec{r})$. Though $V_{\text{int}}(\vec{r})$ is defined over the whole unit cell, it is valid only in the interstitial region. $V_{\text{int}}(\vec{r})$ is found to be:

$$V_{\text{int}}(\vec{r}) = A + V_1 z + 2\pi\rho_{00} z^2 + \sum_{m,n} \frac{4\pi}{\left|\vec{K}\right|^2} e^{i\vec{G}_m \bullet \vec{r}} \begin{Bmatrix} \cos(k_n z) \\ \sin(k_n z) \end{Bmatrix} + \sum_{m \neq 0} \left[V_{m^+} e^{G_m z} + V_{m^-} e^{-G_m z} \right] e^{i\vec{G}_m \bullet \vec{r}} . \tag{2.46}$$

The electrostatic potential in the muffin-tin region, $V_{MT}(\vec{r})$ is found by numerically solving Poisson's equation for $V_{L,\vec{K}}(\vec{r})$. This is accomplished by using the actual charge density in the muffin-tins ρ_{MT} from equation (2.38) and (2.39). The solution has the form:

$$V_{MT}(\vec{r}) = \sum_{\vec{K}} \sum_{L} V_{L,\vec{K}}(\vec{r}) Y_L(\theta,\varphi) \,. \qquad (2.47)$$

F. The Exchange-Correlation Potential

Once the electrostatic potential has been calculated, the only unknown potential term remaining is the exchange-correlation potential $V_{xc}(\vec{r})$. Unfortunately, the value given for $\varepsilon_x([\rho],\vec{r})$ in equation (1.9) systematically underestimates the actual value $\varepsilon_x([\rho],\vec{r})$; and the error worsens as the charge density increases to levels typical of metallic atoms. Perdew and Zunger[10] improved upon $\varepsilon_{xc}([\rho],\vec{r})$ by using a parameterization developed by Ceperley and Alder[11] which more accurately models the behavior of an electron gas at high densities.

Here $\varepsilon_{xc}([\rho],\vec{r})$ is found to be the sum of the exchange energy, $\varepsilon_x([\rho],\vec{r})$, and the correlation energy, $\varepsilon_c([\rho],\vec{r})$; where $\varepsilon_x([\rho],\vec{r})$ is the ordinary Hartree-Fock contribution given in spin polarized form as:

$$\varepsilon_x([\rho],\vec{r}) = -6\left(\frac{3}{4\pi}\right)\frac{\left(\rho^+ + \rho^-\right)^{4/3}}{\rho} \,. \qquad (2.48)$$

Defining r_s as $\frac{4\pi}{3} r_s^{\,3} = \rho^{-1}$, $\varepsilon_c([\rho],\vec{r})$ is parameterized at low densities ($r_s \geq 1$) as:

$$\varepsilon_c([\rho],\vec{r}) = \frac{\gamma}{(1+\beta_1\sqrt{r_s}+\beta_2 r_s}\ . \qquad (2.49)$$

For high densities ($0 \le r_s < 1$), $\varepsilon_c([n],\vec{r})$ is parameterized as:

$$\varepsilon_c([\rho],\vec{r}) = A\ln(r_s) + B + C\ln(r_s) + D\ . \qquad (2.50)$$

The parameterization constants are fixed by evaluating the expression with the known values for $\varepsilon_{xc}([\rho],\vec{r})$ from the fully polarized and unpolarized gases. At intermediate polarizations, the standard interpolation formula of von Barth and Hedin is applied.[12] This gives the correlation energy for a local charge density polarization, $\xi = \frac{\left(\rho^+ - \rho^-\right)}{\rho}$, as:

$$\varepsilon_c([\rho],\vec{r}) = \varepsilon_c{}^U([\rho],\vec{r}) + f(\xi)[\varepsilon_c{}^P([\rho],\vec{r}) - \varepsilon_c{}^U([\rho],\vec{r})] \qquad (2.51)$$

where,

$$f(\xi) = \frac{(1+\xi)^{4/3} + (1-\xi)^{4/3} - 2}{2^{4/3} - 2},$$

and $\varepsilon_c{}^U([\rho],\vec{r})$ and $\varepsilon_c{}^P([\rho],\vec{r})$ are the correlation energies of the unpolarized and polarized electron gases, respectively.

G. Structural Optimization

A common phenomenon exhibited in surfaces is structural relaxation. Due to the absence of some of their neighboring atoms, surface atoms often relax into positions that are unavailable to bulk atoms. These positions,

though not energetically favorable in the bulk, become favorable at the surface where the potential is different.

To investigate the possibility of these relaxed geometries, the total energy required to form the surface arrangement is calculated for various likely geometries. The most favorable geometry is the one lowest in energy.

The total energy functional, $E[\rho]$, is computed for a given structure by taking the expectation value of the Hamiltonian (1.10) with the ground state charge density for that structure, so $E[\rho]$ is given by:

$$E[\rho] = T[\rho] + \int d^3r \left[V_{es}(\rho(\vec{r}),\vec{r}) + \varepsilon_{xc}([\rho],\vec{r})\right]\rho(\vec{r}) - \frac{1}{2}\int d^3\vec{r}\int d^3\vec{r}\,'\frac{\rho(\vec{r})\rho(\vec{r}\,')}{\left|\vec{r}-\vec{r}\,'\right|} + E_{II} \,. \tag{2.52}$$

$\varepsilon_{xc}([\rho],\vec{r})$ is obtained by summing equations (2.48) and (2.51). $V_{es}(\rho,\vec{r})$ for each of the three sub-regions is given by equations (2.41), (2.45), and (2.47). From the positions of the atomic cores in the given structure, E_{II} can be evaluated directly from equation (1.6) for a representative unit cell. Summing the one-electron Schrödinger-like equations given in (1.12) and isolating the kinetic terms yields:

$$T[\rho] = -\frac{1}{2}\sum_i \int d^3r\,\psi_i^{\,*}(\vec{r})\nabla^2\psi_i(\vec{r}) = \sum_i E_i - \int d^3r V_{es}(r)\rho(r) - \int d^3r V_{xc}(r)\rho(r) \,. \tag{2.53}$$

However, the one-electron energy eigenvalues, E_i, are not explicitly computed except for the core electrons. Instead, the density of states is computed from equation (2.25). Therefore, it is more convenient to express the kinetic energy as:

$$T[\rho] = \sum_i E_i + \int dE\, E\sigma(E) - \int d^3 r V_{es}(r)\rho(r) - \int d^3 r V_{xc}(r)\rho(r), \quad (2.54)$$

where the index runs over the core electron states.[11]

Although the SEGF method has proven successful in a number of surface calculations, the number and diversity of surfaces investigated is relatively few in comparison to those employing slab geometries. Thus, application of this method to the Ag(111) surface will present an interesting test of the SEGF method against older slab-based techniques.

CHAPTER THREE

Silver

A. Computational Details

The Ag(111) surface is the most stable surface plane of silver, allowing for easy sample preparation. Consequently, this surface has been the focus of many experimental studies. The large amount of experimental data available is useful for testing the accuracy with which the SEGF method can model surface phenomena. Experimentally observed phenomena include the presence of a slight surface relaxation,[14,15,16] a Shockley-type surface state,[17] and work function measurements.[18]

The crystalline lattice structure of silver is face centered cubic. Experimental x-ray diffraction studies report the length of a side of the cubic lattice to be 7.62 au in the low temperature limit.[19] LDA first principles calculations predict a lattice constant between 7.46-7.88 au.[20,21] The bulk calculation of Moruzzi, Janak, and Williams (MJW) yielded a lattice constant of 7.79 au,[22] a value 2% larger than the experiment. The embedding potential for our SEGF calculation was generated from the MJW bulk potential; so, deviations from the bulk lattice constant

given in the structural study will be reported with respect to the MJW lattice constant.

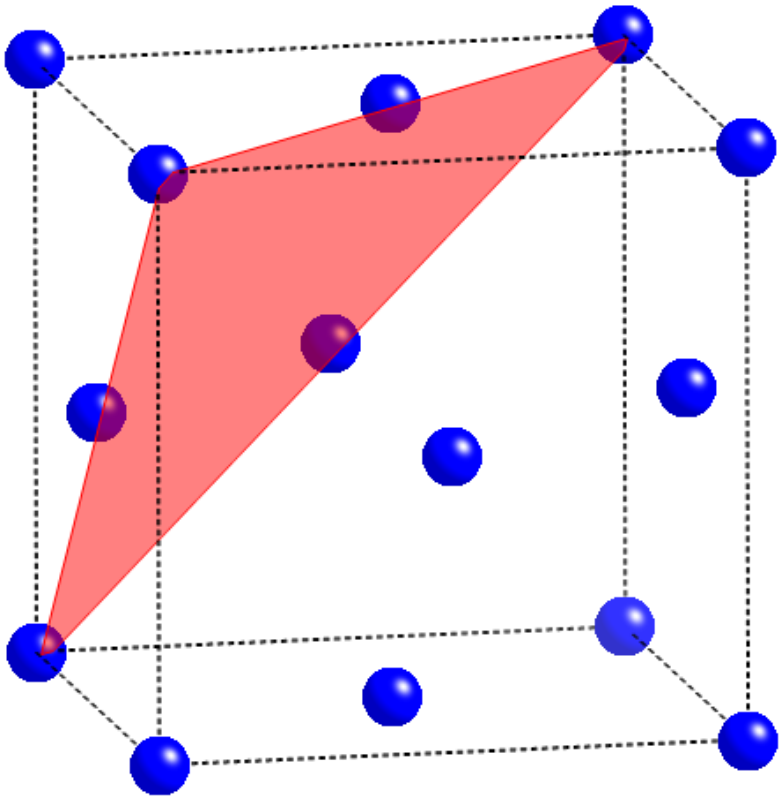

Figure 3.1: The FCC lattice. A (111) plane is highlighted in red.

To model the surface region, a three-layer slab was embedded onto a semi-infinite bulk silver lattice. The (111) slab possesses 3-fold rotational symmetry about any lattice point. The two basis vectors that define the translational symmetry of the (111) surface possesses lengths equal to the nearest-neighbor spacing, and are

oriented at 120^0 with respect to each other (See Figure 3.2a).

From the FCC structure and the MJW lattice parameter an interlayer spacing of 4.50 au and a nearest neighbor distance of 5.51 au was obtained. The muffin-tin radius was chosen to be 2.75 au, so that neighboring muffin-tin spheres touched. Three layers were used in the present calculation; therefore, the height of the unit cell, excluding the vacuum, was 14.50 au. Since there exists an ABC stacking of (111) planes in the FCC structure, the outermost layer resides over the first bulk layer (See Figure 3.2b). The x-y origin was chosen to be centered on an atom in this plane. The origin of the z-axis was chosen to be in the middle of the slab, that is, in the center of the second layer.

The shell structure of a free silver atom possesses a complete 4d shell and a partially-filled 5s orbital. Although the 4d shell is complete in the free atom, the d-electrons in the solid may not be treated as (inert) core electrons since they contribute substantially to the crystalline bonding and lie relatively close to the Fermi energy. Consequently, d-bands are included in the valence structure when calculating electronic properties. With the inclusion of the 5s electron, each Ag atom possesses a

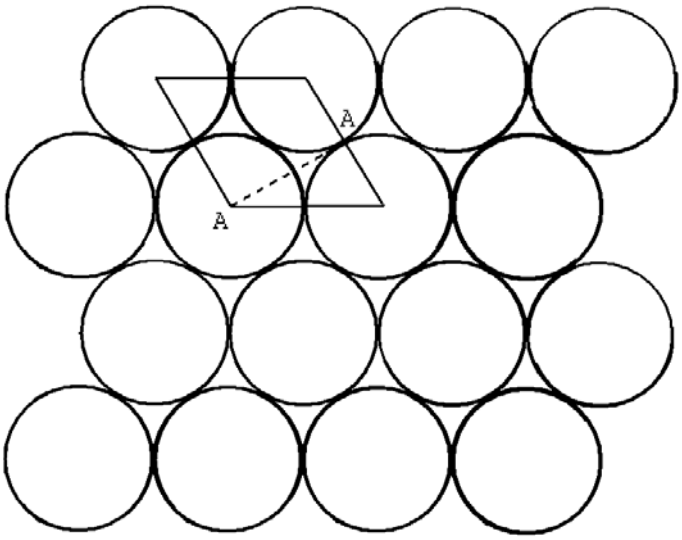

a)

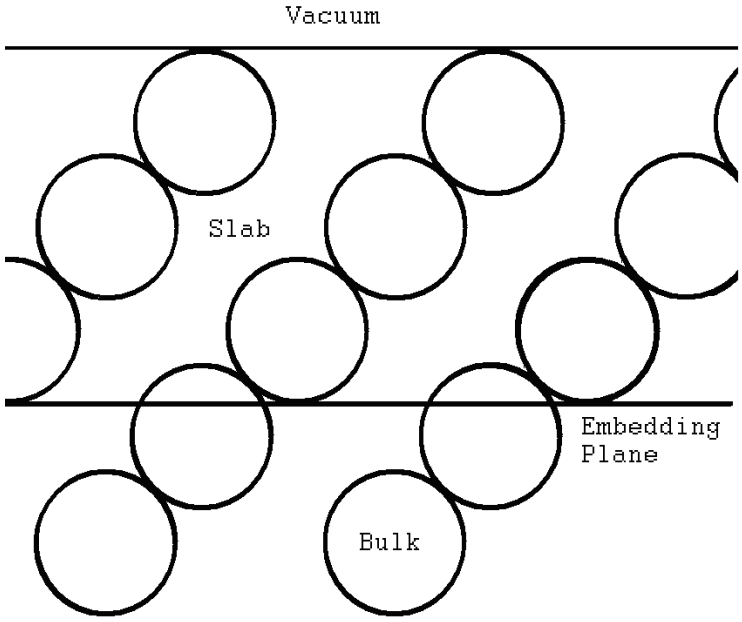

b)

Figure 3.2: Surface geometry. (a) Top View (parallelogram represents the surface unit cell. (b) Side view of the AA vertical plane.

total of eleven valence electrons. With such a large number of electrons per atom and the lack of 2D inversion symmetry, a substantial basis set is required. We have chosen a basis set of fifty LAPW basis functions per atom, or a total of 150 LAPW basis functions for the three-layer slab. To allow sufficient variational freedom at the bulk interface plane, the distance defining the z-component of the LAPW basis was chosen slightly larger than the thickness of the slab.

The number of plane waves used to expand the charge density in the interstitial region was one thousand consisting of 258 star components. Inside the muffin-tins, the charge density was computed on a logarithmic radial grid of 331 points extending up to the muffin tin radius. Angular momentum components up to l=8 were used to expand the charge density and potential inside the muffin-tins. The vacuum region charge density was calculated on a linear mesh of 100 points extending out to 10 au from the surface. This distance was deemed to be sufficient since the charge density at the outermost mesh point was of the order of 10^{-24} electrons/au^3.

A k-point mesh of 36 two-dimensional special k-points was generated using Cunningham's method[23] to sample the

irreducible part of the surface Brillouin zone. The k-point mesh is depicted in Figure 3.3.

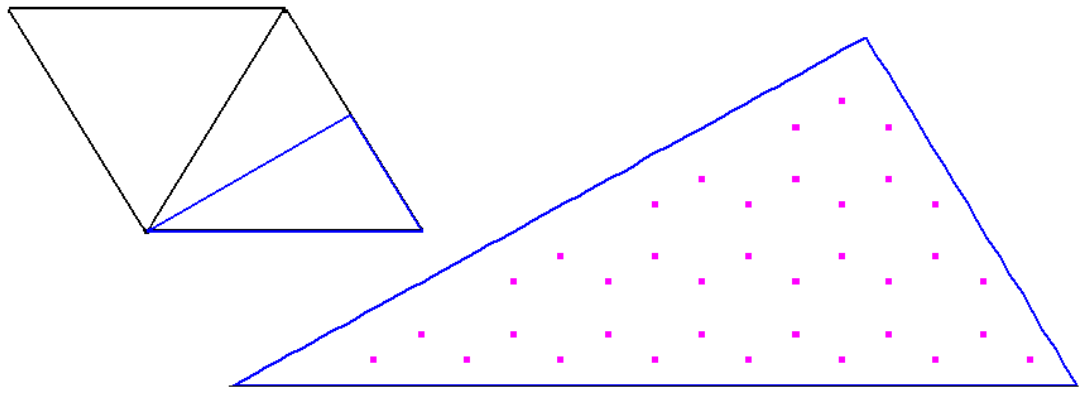

Figure 3.3: The 2D Brillouin zone k-point sampling. The Brillouin zone for a hexagonal crystal is inset in the upper left corner of this figure. Outlined in blue is the irreducible wedge of the Brillouin zone. Inset in the lower right is the irreducible wedge with 36 special k-points selected by Cunningham's method.[23]

In calculating the contour integral of the energy, 31 points were sampled using the Gauss-Chebyshev numerical integration technique. The error in calculating the total charge from sampling 15 or 31 pts was less than 10^{-4} electrons, or eight digits of agreement in charge at any given k-point, which was considered to be adequate convergence.

Since only a finite number of energy points can be sampled in calculating the density of states, a slight imaginary component is added when performing the energy integration. This broadens the delta function behavior the

surface exhibits in occupancy of energy states, allowing for the discrete set of sampling points to adequately represent the density of states. The value for the imaginary part of the energy used was $1*10^{-3}$ Hartree. This value is chosen large enough for adequate numerical stability, and small enough to prevent an artificial broadening of the surface's electronic states energy distribution.

The embedding plane was placed just below the third-layer's muffin-tin sphere at 7.25 au in the z-direction (into the crystal). In this position, the embedding plane is not symmetrically located between atomic planes; thus, the potential varies more widely along the surface than for an embedding plane placed midway between layers. However, this placement prevents a numerical instability (called ghost bands) that occurs for certain choices of LAPW bases when the embedding plane is placed symmetrically between layers.[4] The value of the potential along the embedding plane was chosen to be equal to the potential zero in the bulk calculation. Fifty randomly selected points were sampled along this plane and used to fit the potential.

In expanding the embedding potential, a total of 37 plane waves were used. This small number has been found to be sufficient for expansions limited to the interstitial

region. The bulk embedding potential was computed from the spherically-averaged bulk muffin-tin potential, combined with a constant interstitial potential. For the surface calculation, the full potential, with no shape approximation, was used. Since the bulk interstitial potential is constant and the surface potential is not, there is a slight distortion in the charge density that most affects the layer nearest to the embedding plane. Three layers proved sufficient to screen this imperfection, so that the topmost layer is unperturbed by the slight mismatch in potential.

The exchange-correlation potential and energy were found by using the interpolation method of Ceperley and Alder.[11] The exchange-correlation potential was fitted in the interstitial region for the first 150 star coefficients with 400 randomly selected points. This fitting resulted in a least squares error of $1.8*10^{-4}$ Hartree for the exchange correlation energy. For the muffin-tin region, a Taylor series expansion was made about the spherically-averaged radial charge density out to first order. Likewise in the vacuum region, a Taylor series expansion was made to first order by using the z-planar-averaged charge density.

B. Surface Relaxation

To investigate the presence of surface relaxation on the Ag (111) surface, the total energy of 15 different lattice spacings was computed. To prevent the muffin-tin of the outermost layer from protruding into the vacuum region for an expanded interlayer spacing or from overlapping neighboring muffin-tins upon contraction, the muffin-tin radius of the outermost layer was reduced by 14%. The surface relaxation for the current work is given as a percentage of the bulk layer spacing of 4.50 au. Negative values represent contraction, whereas positive values indicate expansion of the interlayer spacing.

The root mean square (RMS) error between successive potentials was calculated as a measure of convergence. All trials were considered converged when an RMS iteration error below $5*10^{-10}$ Hartree was achieved. The convergence of total energy with iteration error is depicted in Figure 3.4.

By varying the spacing of the outermost layer, an energy minimum was detected near a 0.5% contraction, corresponding to a layer spacing of 4.48 au. For this spacing, the total energy was calculated to be -15921.2102 Hartree. The contraction of 0.5% represents only a slight

deviation from the bulk interlayer spacing. Since the top layer's deviation was so slight, no investigation of a

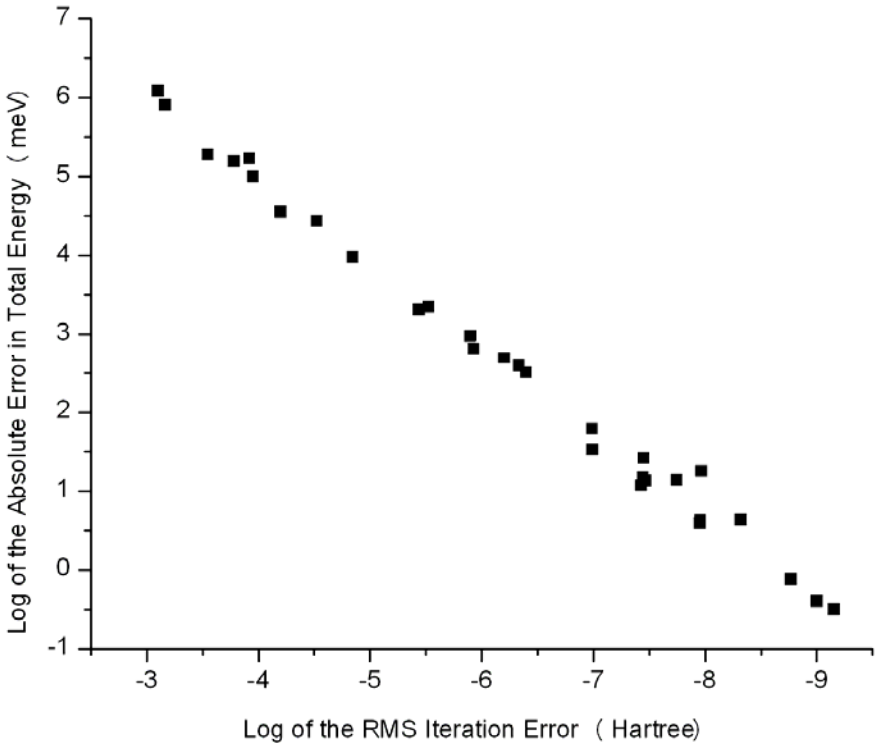

Figure 3.4: The dependence of total energy on RMS iteration error. By converging to within $5*10^{-10}$ Hartree in successive potentials, we see the total energy converge to deviations on the order of a few tenths of an eV.

multilayer relaxation was undertaken. The total energy's dependence with interlayer spacing is presented in Figure 3.5. Prior theoretical investigations have been conducted on the (111) plane of silver. A slab calculation was performed in which the semi-infinite geometry of the surface was replaced by a repeated slab geometry consisting

of a sequence of seven layers of atoms separated by five layers of vacuum. Two studies using differing implementations of the embedded atom method (EAM) have also been conducted. In the EAM, an approximate pair-wise potential is generated

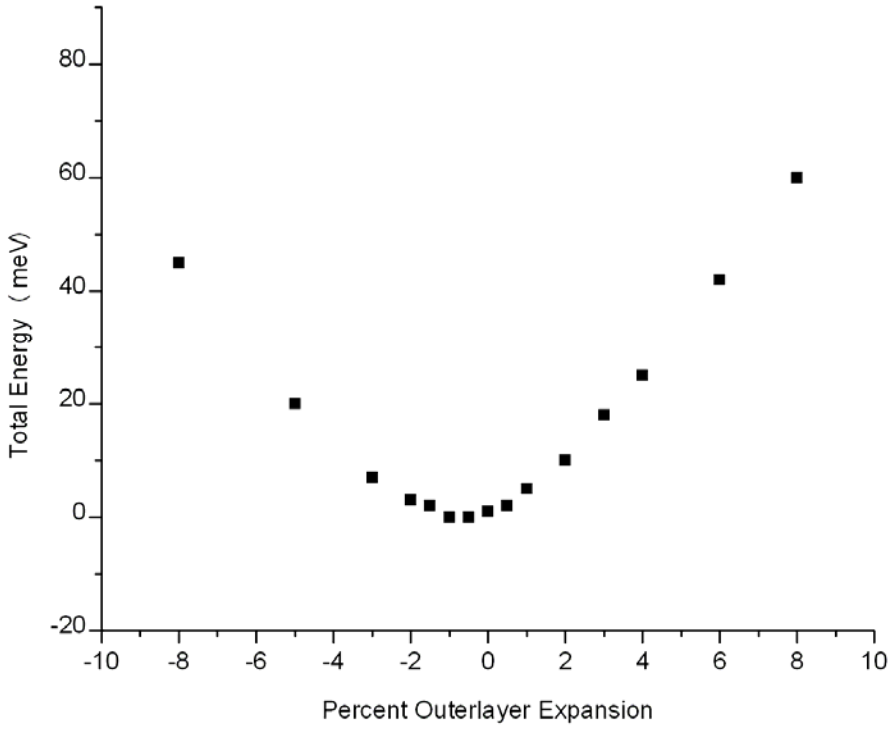

Figure 3.5: Dependence of the total energy on outer layer position. Energy values are given with respect to their deviation from the energy minimum value -15921.2102 Hartree.

between the surface region atoms and the first few nearest neighbor atoms in the bulk. Another study utilizing the Linearized Muffin-Tin Orbital method within the Atomic Spheres Approximation (LMTO-ASA) has also been conducted.

The basis set within the LMTO differs from the plane wave basis utilized in our calculation. This choice of basis greatly complicates the solution of the electrostatic potential, so a shape approximation is made where the potential is taken to be the potential of that generated from a spherically averaged charge density. In addition to the shape approximation of the potential the semi-infinite geometry of the surface is treated in the repeated slab geometry of seven layers of atoms separated by ten layers of vacuum.

Though the predicted 0.5% contraction of the current study is smaller than prior theoretical investigations, it is closer to the observed value. Experimental results of Low Energy Electron Diffraction (LEED) and High Energy Ion Scattering (HEIS) both indicate a 0.0% contraction.[14,15]. However, a Medium Energy Ion Scattering (MEIS) experiment measured a 2.5% contraction of the outermost layer of Silver, in contrast to the LEED and HEIS results.[16] Thus, the best agreement is then found with the current theoretical model and these experimental results

The results of experimental and theoretical studies on the two outermost layers of the Ag(111) surface are summarized in Table 3.1. Thus, the best agreement is then found with the current theoretical model and these

Table 3.1: Comparison of the present calculated interlayer expansion with other theoretical and experimental values. d_{12} denotes the interlayer spacing change between the first and second layers. All values are given as a percent deviation from the equilibrium lattice constant.

Technique	d_{12}	d_{23}
Present work	-0.5	*
LEED experiment[14]	0.0	0.0
HEIS experiment[15]	0.0	*
MEIS experiment[16]	-2.5	0.6
Embedded atom method[24]	-1.2	0.5
LMTO-ASA 7+10vac[25]	-1.5	0.1
Embedded atom method[26]	0.94	-0.07
Slab 7+5vac[27]	-1.0	-0.2

experimental results. A possible source of error impacting the current study's prediction of the Ag(111) surface relaxation is the inaccuracy in the bulk lattice constant imported from the MJW bulk calculation. Since the contraction of the top layer is so slight, the 2% deviation between the MJW bulk interlayer spacing and experiment is of the order of reduction found in the surface interlayer spacing compared to the bulk interlayer spacing witnessed in other experimental and theoretical studies.

C. Charge Density

Compared to atoms in the infinite crystal the semi-infinite crystal can show charge depletion in atoms near the surface. This depletion is caused by the difference in potential electrons near the surface experience. However, the Fermi energy should be unperturbed from the bulk value, since the number of bulk layers dwarfs the surface region, creating an adequate thermodynamic reservoir of electrons. Thus, to calculate the charge density, the surface Green function is integrated up to the bulk Fermi energy to determine the surface occupancy, rather than artificially requiring charge neutrality. The charge density was said to have achieved self-consistency when the RMS error in potentials was less than $5*10^{-10}$ Hartree. For the optimal

structural parameters, a total valence charge density of 32.96 electrons was found for three surface layers indicating a depletion of charge in the surface region of 0.04 electrons with respect to the bulk.

The total valence charge residing in the vacuum region was found to be 0.09 electrons, and a total of 3.28 electrons resided in the interstitial region.

The total valence charge density is illustrated in Figure 3.6. The average interstitial charge density was found to be 0.004 electrons/au^3. Constant density contours were then found by starting from the average interstitial charge density in steps of this density up to a density of 0.06 electrons/au^3. The results were plotted in Figure 3.6 to illustrate the charge density variations in the Ag(111) surface. At the bottom of the figure, the appearance of a fourth layer can be observed. It is interesting to note that this layer is not actually present in the calculation- its appearance is due to the bulk embedding potential and illustrates the influence the bulk region has on the embedded surface region.

D. Work Function

The work function is measured using a photoemission spectrometer (Figure 3.7). A monochromatic light source

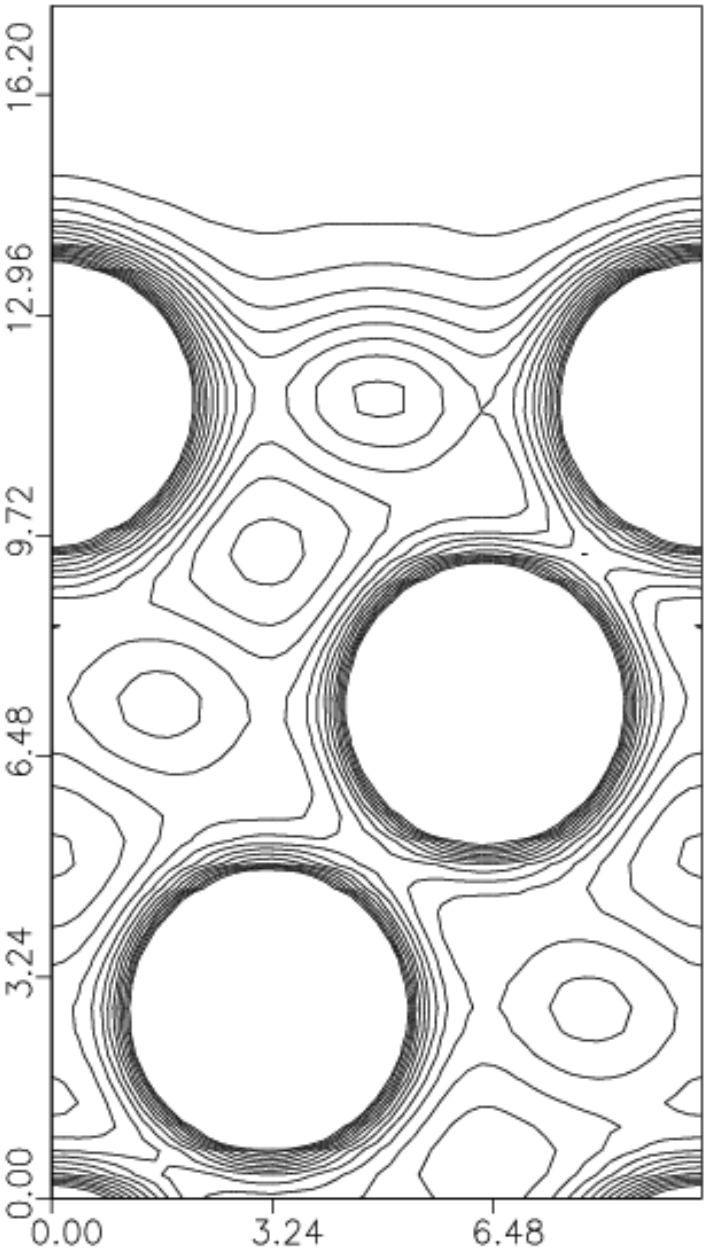

Figure 3.6: Self-consistent Ag(111) total charge density in a vertical plane across a unit cell. (The vacuum is at the top of the figure). Distances are measured from the embedding plane and are given in au.

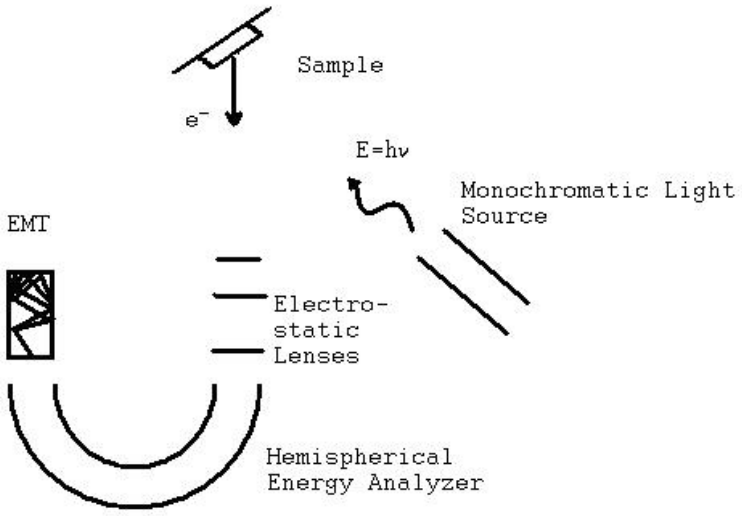

Figure 3.7: Diagram of a photoemission spectrometer.

with $E = h\nu$ shines light on a sample. This produces electrons via the photoelectric effect. Electrons entering the surface at polar angle θ, and azimuthal angle ϕ, are focused through an electrostatic lens and passed through a hemispherical electrostatic analyzer. This allows electrons of only a particular kinetic energy to pass, and the resulting current of these electrons is measured with the aid of an electron multiplier tube. Light, viewed as a stream of photons with a well defined energy, impinges on the surface, exciting some of the electrons within the surface. If the electrons are weakly bound to the surface, they can be emitted. An energy analyzer detects the electron current as a function of kinetic energy. The emitted electrons having the greatest kinetic energy are

those most weakly bound to the surface. The difference between the photon energy and the highest observed kinetic energy of emitted electrons is the work function: the minimum amount of energy required to remove an electron from the surface.

The experimental precision of the hemispherical electrostatic energy analyzer limits experimental precision to approximately one hundredth of an eV. Yet, systematic uncertainties in sample preparation and cleanliness of the surface can greatly affect the ultimate precision of the measurement. Using photoemission spectroscopy, Dweydari and Mee found the Ag(111) work function to be 4.74 eV.[18]

As discussed in Chapter 2, the work function was calculated theoretically by taking the difference in the vacuum constant and the Fermi energy. As can be seen in Figure 3.8, the calculated work function proved to be largely insensitive to the outer layer displacement, since a 16% change in lattice size altered the work function value by less than 2%. By taking the relaxed geometry found from the total energy calculation, a theoretical work function for Ag was found to be 4.745 eV, which compares extremely well with the experimental value of 4.74 eV.

In performing the self-consistent calculations, the work function was converged more rapidly than the total

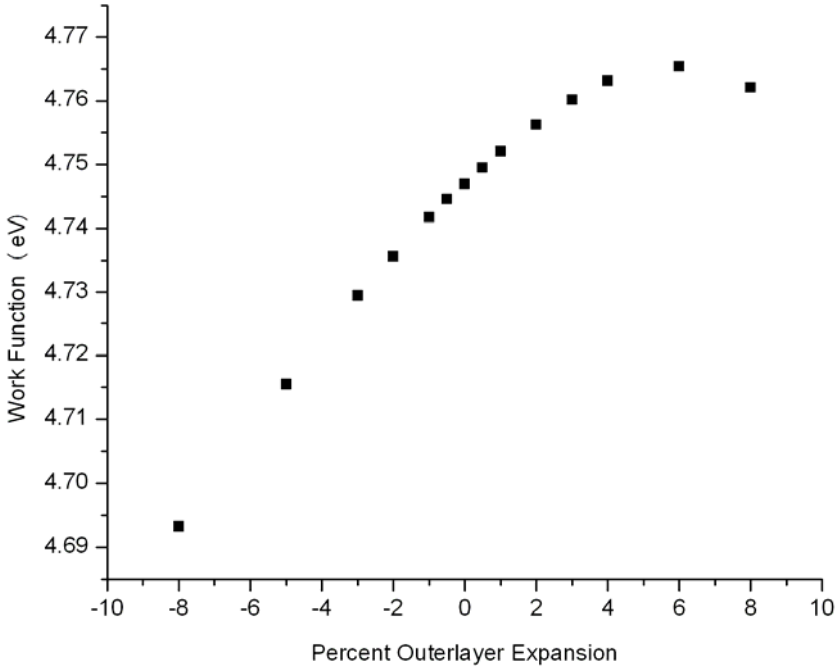

Figure 3.8: Dependence of work function on outer layer expansion.

energy as can be seen in Figure 3.9. For the total energy, convergence was achieved when the RMS error in successive potentials was on the order of 10^{-10} Hartrees. For the work function, convergence to within 0.1 eV was obtained when the RMS error in successive potentials was still of the order of 10^{-7} Hartrees.

Other theoretical work function studies have been conducted for the work function of Ag(111) (Table 3.2). A slab calculation was performed using 7 atomic layers

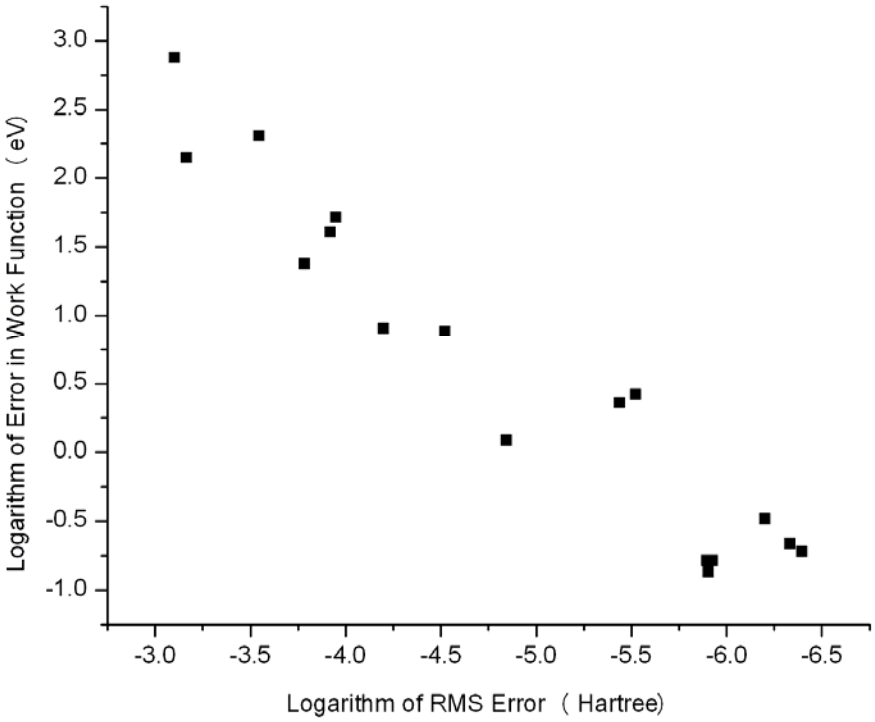

Figure 3.9: Dependence of the error in work function with RMS error in successive potentials.

separated by 5 vacuum layers.[28] A prior SEGF study with an LAPW basis of Ishida was conducted using 2 slab layers, and neglecting structural relaxations.[8] Another SEGF study utilizing a Linearized Muffin-Tin Orbitals basis set within the Atomic Sphere Approximation (LMTO-ASA) was performed with four layers of atoms and two of vacuum and no structural relaxation, to model the (111) surface of silver.[29]

Table 3.2: Comparison of calculated the Ag(111) work functions with the experimentally determined value.

	Work function for the Ag(111) surface
Present work	4.75 eV
Experiment[18]	4.74 eV
Seven-layer slab[28]	4.67 eV
LMTO-SEGF four-layer[29]	5.01 eV
SEGF two-layer[8]	4.97 eV

The present results are in better agreement with experiment than all previous theoretical work (Table 3.2). Earlier SEGF studies overestimated the work function by more than two tenths of an eV. This study provides no evidence of the SEGF method overestimating the work function in the case of silver. Errors obtained in calculating the work function in prior studies appear to be from the implementation of the SEGF method.

However, the level of agreement with experiment and this study exhibits is somewhat fortuitous, as there is an uncertainty introduced in the calculation based on the finite size of the LAPW basis functions. Figure 3.10 illustrates the convergence of the work function with LAPW basis size for a calculation utilizing 2 slab layers. From

this analysis the estimated error in the work function from finite basis size could be as large as 0.05 eV.

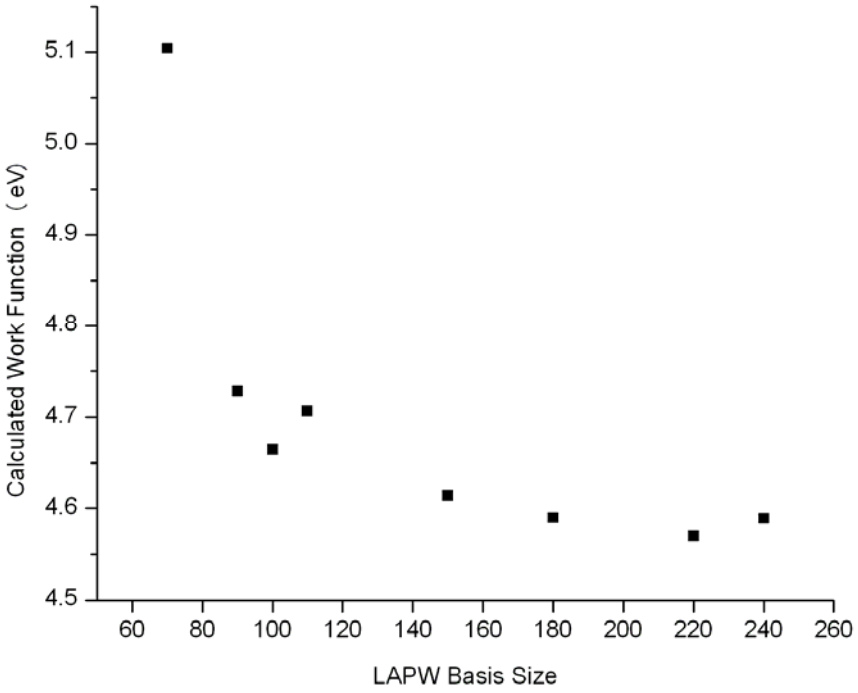

Figure 3.10: Calculated work function dependence on LAPW basis size. For a two-layer slab with no relaxation in atomic positions, the basis size was extended up to 240 LAPWS, illustrating the influence of basis size on computed work function. Due to computational time limits, extending the basis size further than 150 LAPWs to show convergence for a three-layer slab would be impractical.

Further error could have occured by enforcing bulk behavior after only 3-layers. Since the difference in work function between 2 and 3 layers was found to be on the order of one tenth an eV, as Figure 3.10 also demonstrates, the error in modeling the semi-infinite crystal with only

three layers deviating from bulk behavior is estimated as less than a tenth of an eV.

E. Density of States

The Density of States (DOS) is defined as the number of electronic states per unit energy. Although no direct measurement is possible, photoemission spectroscopy allows experimenters to indirectly probe the density of states. Figure 3.7 displays a typical photoemission experimental setup. As the spectrometer scans across kinetic energies, intensity variations in the electron beam are observed. The trajectories of excited electrons are determined from the momentum possessed in the surface region before excitation. By mapping the intensity of excited electrons across differing trajectories, the density of states as a function of k-space may be found, and by integrating across the whole space of trajectories, an image of the total density of states may be found. However, due to the difficulty of experimental resolution, precise measurement for one particular k-point is not possible; instead, a small region of k-space is sampled.

Surface states are detectable features of photoemission spectra. These states arise from the loss of the bulk Born-von Karman boundary conditions allowing for

non-periodic solutions of Schrödinger's equation. Surface states fall into two classes. One type, called Tamm states, typically possess small decay lengths and are located in the center of bulk band gaps. The second type are called Shockley states. Shockley states generally have longer decay lengths and may have large amplitudes in interior layers.

Kevan and Gaylord reported observing a Shockley surface state when investigating the photoemission spectrum of Ag (see Figure 3.11).[17]

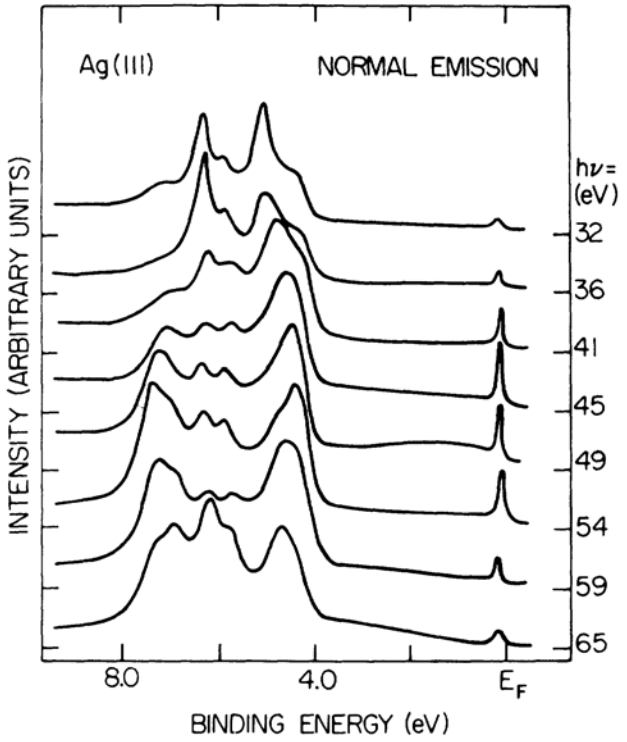

Figure 3.11: Experimental Ag(111) UPS spectra taken by Kevan and Gaylord.[17] The $\overline{\Gamma}$ surface state is observed as a peak just below the Fermi energy. Located further below this state are the 4d-bands of silver.

The feature observed just below the Fermi energy in Figure 3.11 is the Shockley surface state that exists near $\overline{\Gamma}$. This surface state is located at 0.12±0.01 eV below the Fermi level.[17] Theoretically, the total DOS in the surface region is given by Equation 2.25. In evaluating the total DOS, we may choose to integrate across only a particular region of space; this allows for us to investigate the contributions to the DOS arising from different localities.

In Figure 3.12, the $\overline{\Gamma}$ DOS contributions for various regions are plotted. The DOS for the surface region near $\overline{\Gamma}$ still possesses sharp delta function-like peaks. This indicates the value of $1*10^{-3}$ Hartree for the imaginary part of the energy is properly chosen. A surface state is clearly observed at 0.22 eV below the Fermi level. By analyzing the relative amplitude of the surface state peak to other features in the DOS near the first point in the vacuum region, the surface state is clearly observed as the dominant occupied state. The surface state is present throughout the entire surface region, reaching a maximum in muffin-tins of the second layer. Inside the muffin-tins of the third layer, located nearest to the embedding plane of the bulk, the surface state occupancy is relatively small compared to features deeper in the valence band. This

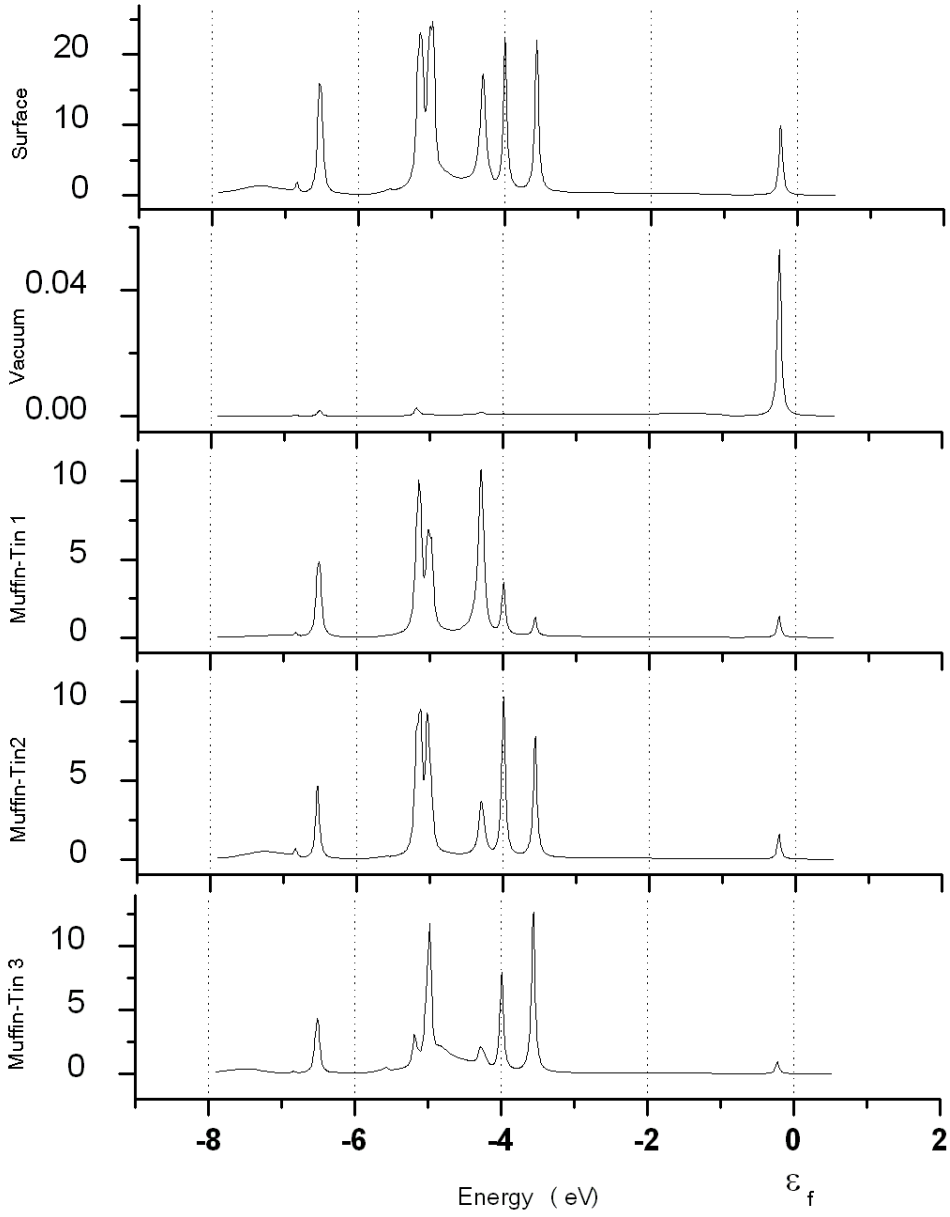

Figure 3.12: The DOS at $\bar{\Gamma}$ for the surface region and for each sub-region of the surface. Note the difference in scaling for vacuum and total surface regions.

indicates the decay of the surface state into the bulk. From the bulk band structure provided by MJW, the location of the surface state is within the s-p bulk band gap of Ag, and is a true surface state.

By assuming a 5^{o} uncertainty in emission angle and an emitted electron energy of 40 eV, an electron wave number of 1.72 au^{-1} was found to sweep a radius of 0.15 au^{-1} in the 2-D Brillouin zone. On a regular grid, 19 K-points were sampled in the irreducible wedge of the 2-D Brillouin zone.

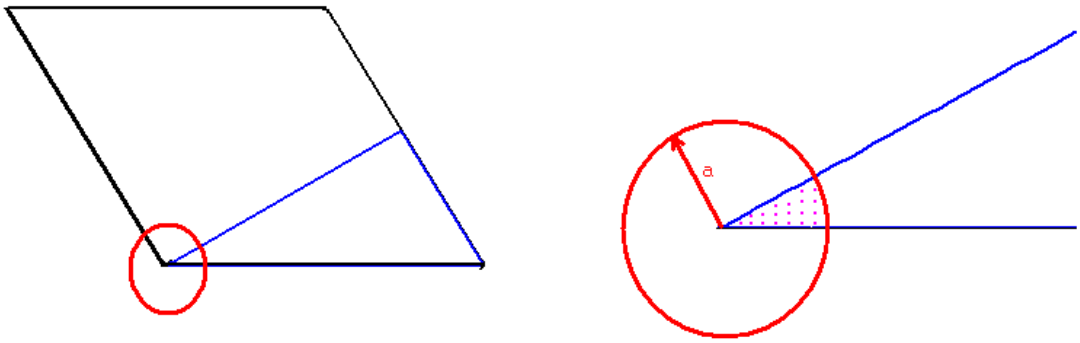

Figure 3.13: Selection of k-points to determine the behavior of the surface state near $\bar{\Gamma}$. The irreducible wedge of the Brillouin zone is highlighted in blue. The annulus of k-space sampled by the experiment is highlighted in red.

The surface state peak in this region of k-space was computed to occur at 0.15 eV below the Fermi energy. This shows a discrepancy in the location of the surface state of 0.03 eV. A prior theoretical study,[30] using the direct-transition model based on the bulk states reported a predicted value of 0.19 eV. This indicates the more

accurate treatment of the surface undertaken in the SEGF method.

By summing over a total of 36 special k-points in the 2-D Brillouin zone, the total density of states was calculated for the surface region. Since the entire 2-D Brillouin zone is sampled to generate the total DOS, each k-point DOS is averaged together. Near $\bar{\Gamma}$ this state is a surface state, yet away from $\bar{\Gamma}$ the surface state transitions to a surface resonance above the Fermi energy. So, in the total density of states, the surface peak is seen lying unoccupied above the Fermi energy. This resonance is not observable through photoemission spectroscopy, since there is no electron residing in the states above the Fermi energy. Instead, it can be detected by inverse photoemission spectroscopy. In inverse photoemission spectroscopy, an electron incident to the surface becomes trapped in the surface potential and emits a photon to conserve energy. The difference in the emitted photon energy and incident electron energy is the change in potential of the electron.

From Figure 3.14, a surface resonance is predicted to be observed at 0.26 eV above the Fermi energy. Figure 3.15 illustrates the results of a k-resolved inverse photoemission spectrum.[31] The feature located just above

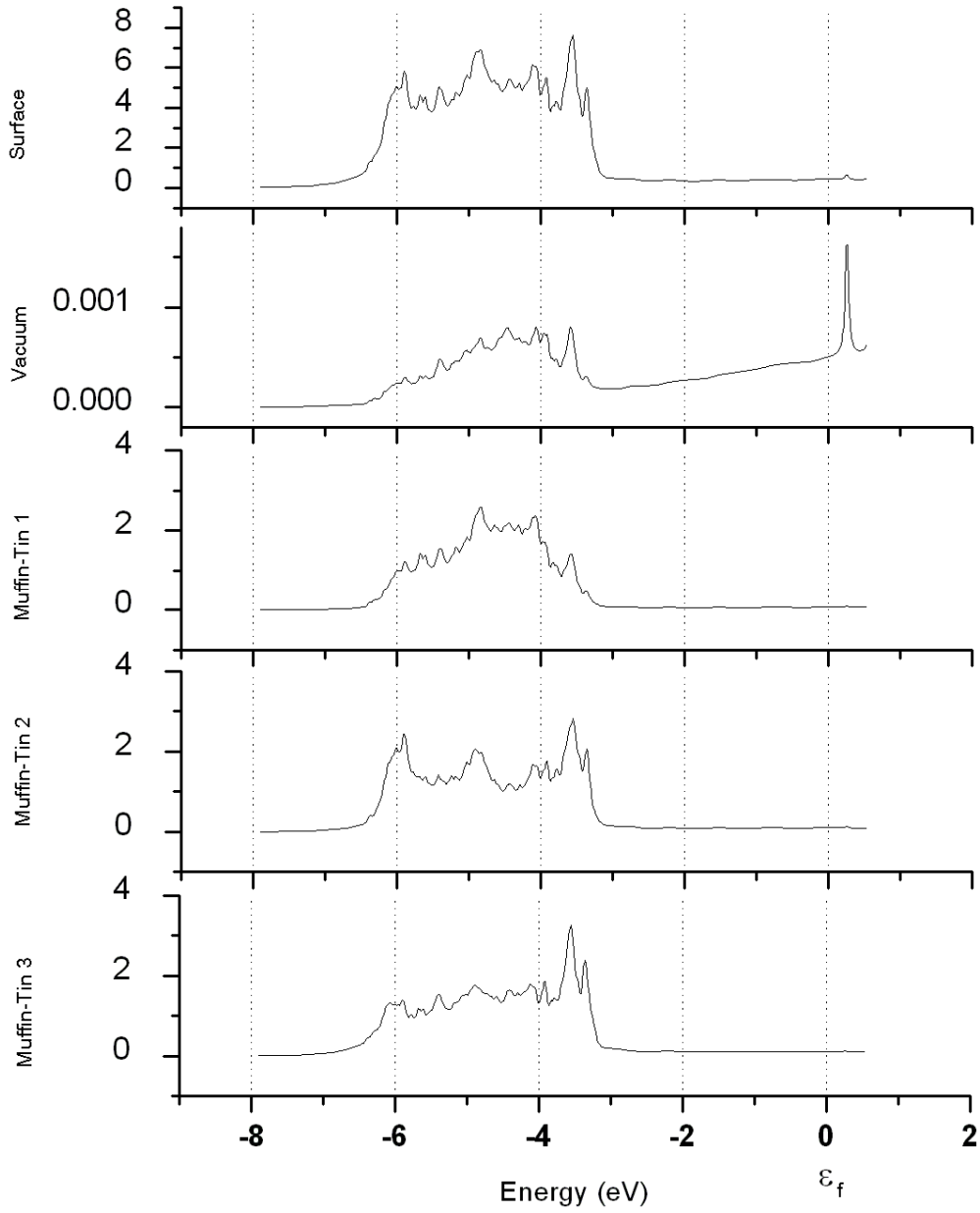

Figure 3.14: Total density of states. For the surface region and for each sub-region of the surface the occupancy in states per eV is plotted against energy as measured from the Fermi energy. Generated by sampling 36 special k-points smoothing of the surface DOS into a continuous spectrum is clearly visible.

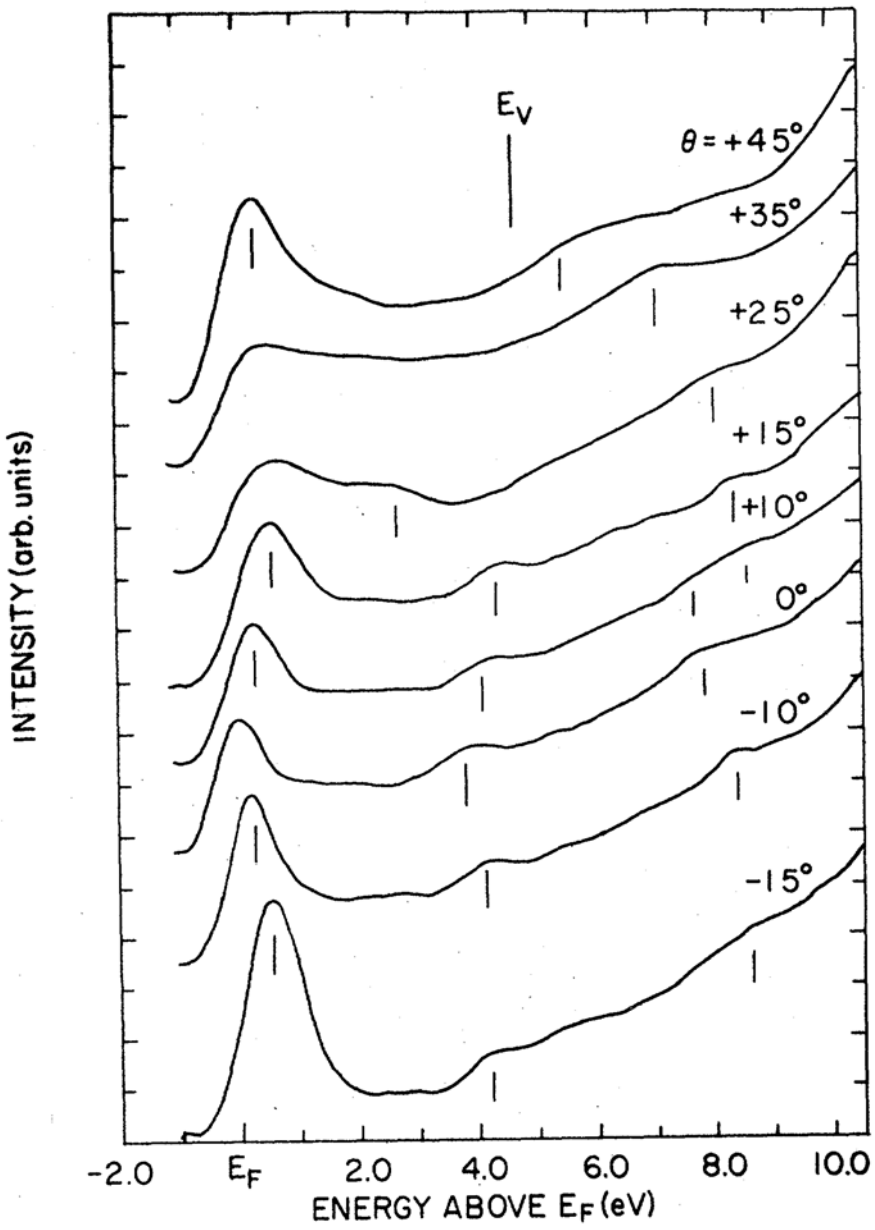

Figure 3.15: Experimental k-resolved inverse photoemission spectrogram of the Ag(111) surface.[31] Using a fixed photon energy of 9.7 eV along the $\overline{\Gamma}$ - $\overline{K}$ direction.

the Fermi energy is a surface resonance having a slight k-dependence sweeping a region from 0.1 eV near $\overline{\Gamma}$ to 0.5 eV. Considering the full width at half maximum in the inverse photoemission spectrum, this represents excellent agreement.

Prior SEGF studies have failed in attempts to recreate realistic total densities of states.[32,33] Methods included either artificial broadening the observed peaks or by summing k-points. The k-point summation method has been demonstrated to work on the Ag surface, and could be utilized on other surfaces. The primary requisite to successfully employing the k-point summation method is that an adequate number of k-points be summed.

F. Conclusion

The Ag(111) surface has been successfully examined by means of the SEGF method. A reasonable prediction of the relaxed surface geometry has been made by computing the geometry having the least energy. Although prior SEGF investigations overestimated the work function of the Ag(111) surface, the current study predicts a work function in excellent agreement with experiment. No evidence is found of systematic errors in applying the SEGF method to the Ag(111) surface. The method as implemented produces

exceptional agreement with observed photo-electron spectroscopy data. In investigating the energetics of surface states, the best agreement has been found with experiment using the SEGF method as opposed to other theoretical methods. Also, a method for accurately generating the total DOS for the surface region has been successfully implemented.

The excellent treatment of the Ag(111) surface by the SEGF method warrants investigation into the interaction adatoms have with the surface. In particular, atomic oxygen is known experimentally to form an ordered overlayer on the Ag(111) surface.[34] By modeling this surface, the accuracy the SEGF method could be tested on more diverse surface phenomena, such as the activation energy for desorption of oxygen from the Ag(111) surface or the changes in electronic structure induced on the Ag(111) substrate from the presence of the oxygen. Also, analysis of the energy barriers of hydrogen diffusion across the Ag(111) surface would be of interest to experimenters utilizing inelastic electron tunneling spectroscopy, since either the prior theoretical model inaccurately treated the surface or are not consistent with our current understanding of surface diffusion.

REFERENCES

1. P. Hohenberg and W. Kohn, Phys. Rev. 136 864, 1964.

2. W. Kohn and L. J. Sham Phys. Rev. 140 1133, 1965.

3. G. A. Benesh, J. E. Inglesfield, Phys. Rev. B 37 6682, (1988).

4. G. A. Benesh, J. E. Inglesfield, J.Phys. C 17, 1595 (1984).

5. G. A. Benesh, L. S. G. Liyanage, J.C. Pingel, J. Phys.: Condens. Matter 2 9065-9076, 1990.

6. O. K. Anderson,Phys. Rev. B 12 3060, 1975.

7. M. A. Van Hove, R. J. Koestner, P. C. Stair, J. P. Biberian, L. L. Kesmodel, I. Bartos, and G. A. Somororjai, Surf. Sci. 103 189, (1981).

8. H. Ishida, Phys. Rev. B 63, 165409 (2001).

9. M. J. Weinert, Math. Phys. 22, 2433 (1981)

10. J. P. Perdew and A. Zunger, Phys. Rev. B 23, 5048 (1981).

11. D. M. Ceperley and B. J. Alder, Phys. Rev. Lett. 45, 566 (1980).

12. U. von Barth and L. Hedin, J. Phys. C 5, 1629 (1972).

13. G. A. Benesh and D. Gebreselasie, Phys. Rev. B 54 5940, (1996).

14. P. Statiris, H. C. Lu, and T. Gustafsson, Phys. Rev. Lett. 72, 3574 (1994).

15. F. Soria, J. L. Sacedon, P. M. Echenique, and D. Titterington, Surf. Sci. 68, 448 (1977).

16. R. J. Culbertson, L. C. Feldman, P. J. Silverman, and H. Boehm, Phys. Rev. Lett. 47, 657 (1981).

17. S. D. Kevan and R. H. Gaylord, Phys. Rev. B 15, 5809 (1988).

18. A. W. Dweydari and C. H. B. Mee, Phys. Status Solidi A 27, 223 (1975).

19. P. Villars and L. D. Calver, *Pearson's Handbook of Crystallographic Data for Intermetallic Phases* (American Society for Metals, Metals Park, OH, 1991).

20. A. Klein, D. J. Singh, and C. J. Umrigar, Phys. Rev. B 51, 4105 (1995).

21. M. Asato, A. Settels, T. Hoshino, T. Asada, S. Blügel, R. Zeller, and P. H. Dederichs, Phys. Rev. B 60, 5202 1999.

22. V. L. Moruzzi, J. F. Janak, and A. R. Williams, *Calculated Electronic Properties of Metals,* (Peragmon, New York, 1978).

23. S. L. Cunningham, Phys. Rev. B 10, 4988 (1974).

24. S. M. Foiles, M. I. Baskes, and M. S. Daw, Phys. Rev. B 33, 7983 (1986).

25. M. Methfessel, D. Hennig, and M. Sheffler, Phys. Rev. B 46, 4816 (1992).

26. J. Wan, Y. L. Fan, D. W. Gong, S. G. Shen, X. Q. Fan, Modeling Simul. Mater. Sci. Eng. 7, 189 (1999).

27. J. Xie, S. Gironcoli, S. Baroni, M. Scheffler, Phys. Rev. B 59, 970 (1999).

28. H. L. Skriver and N. M. Rosengaard, Phys. Rev. B 46, 7157 (1992).

29. H. M. Polatoglou, M. Methfessel, and M. Scheffler, Phys. Rev. B 48, 1877 (1993).

30. S. G. Louie, P. Thiry, R. Pinchaux, Y. Petroff, D. Chandesris, and J. Lecante, Phys. Rev. Lett. 44, 549 (1980).

31. S. L. Hulbert, P. D. Johnson, N. G. Stoffel, and N. V. Smith, Phys. Rev. B 32, 3451 (1985).

32. G. A. Benesh and L. S. G. Liyanage, Surf. Sci. 261, 207 (1992).

33. G. A. Benesh and L. S. G. Liyanage, Phys. Rev. B 49, 17264 (1994).

34. G. Rovida, F. Pratesi, M. Maglietta, and E. Ferroni, Surf. Sci. 43, 230 (1974).